RESEARCH ARTICLE SUMMARY

NEUROSCIENCE

A whole-brain single-cell atlas of circadian neural activity in mice

Katsunari Yamashita†, Fukuaki L. Kinoshita†, Shota Y. Yoshida, Katsuhiko Matsumoto, Tomoki T. Mitani, Hiroshi Fujishima, Yoichi Minami, Eiichi Morii, Rikuhiro G. Yamada, Seiji Okada, Hiroki R. Ueda

Full article and list of author affiliations:
https://doi.org/10.1126/science.aea3381

INTRODUCTION: Neural activity across different brain regions underlies essential physiological and behavioral functions. These activities are coordinated in space and time, and circadian rhythms are a fundamental temporal regulator of such activity, influencing sleep, metabolism, hormone secretion, and cognition. Although the suprachiasmatic nucleus (SCN) has been extensively studied as the master pacemaker, how spontaneous neural activity is coordinated across the entire brain over the circadian cycle has remained elusive. Previous approaches, including electrophysiological recordings, in situ hybridization, immediate early gene labeling, circadian gene reporters, and calcium imaging, have typically been restricted to limited regions and lack spatial continuity, making it difficult to achieve a systematic view.

RATIONALE: To overcome these limitations, we used tissue clearing and three-dimensional whole-brain c-Fos immunostaining. c-Fos is notable for its rapid and broad induction across the brain, making it suitable for spatially comprehensive mapping of neural activity. By sampling brains every 4 hours over 2 days under constant darkness, we aimed to generate a whole-brain atlas of circadian neural activity at single-cell resolution and to identify how different regions and subregions contribute to the temporal organization of brain function.

RESULTS: Each brain contained between 0.4 and 3.0 million c-Fos–positive cells. Time-series analysis of 144 brains revealed that 79% of 642 anatomically defined regions showed significant circadian rhythmicity. Most regions peaked during the late subjective night, corresponding to the active phase in nocturnal mice, whereas some, including sleep-promoting nuclei such as the ventrolateral preoptic area, peaked during the subjective day. Visual regions peaked during the daytime, in antiphase to auditory regions at night, highlighting functional specialization. The hippocampal memory system showed notable internal diversity: CA1 and CA3 peaked during the active phase, whereas the dentate gyrus peaked during the inactive phase, nearly in antiphase. This inversion aligns with reports of dentate gyrus recruitment during sleep stages, suggesting phase-specific contributions to memory processing. Voxelwise analysis further revealed distinct subregional dynamics, including heterogeneous patterns in the SCN and dorsomedial nucleus of the hypothalamus, and a gradual peak time shift along the dorsoventral axis within CA1, highlighting continuous spatiotemporal variation even within single structures. In addition, we demonstrated that whole-brain c-Fos activity patterns could accurately predict circadian time using computational approaches adapted from omics data, confirming that brain-wide rhythms collectively encode temporal information.

CONCLUSION: Our study establishes a comprehensive atlas of circadian neural activity at the whole-brain scale. By combining tissue clearing with large-scale time-series sampling and systematic quantitative analysis, we provide a global view of how neural activity rhythms are organized across hundreds of regions and subregions. The open-access database we developed allows users to explore these rhythms by region or voxel and to upload custom regions of interest for analysis. It is designed to be compatible with gene expression, connectivity, and cell-type resources, enabling integrative analyses that link circadian activity with molecular and anatomical data. Thus, this resource not only advances chronobiology but also provides a temporal framework across neuroscience, linking time-of-day dynamics to studies of diverse brain functions, pharmacology, and disease. □

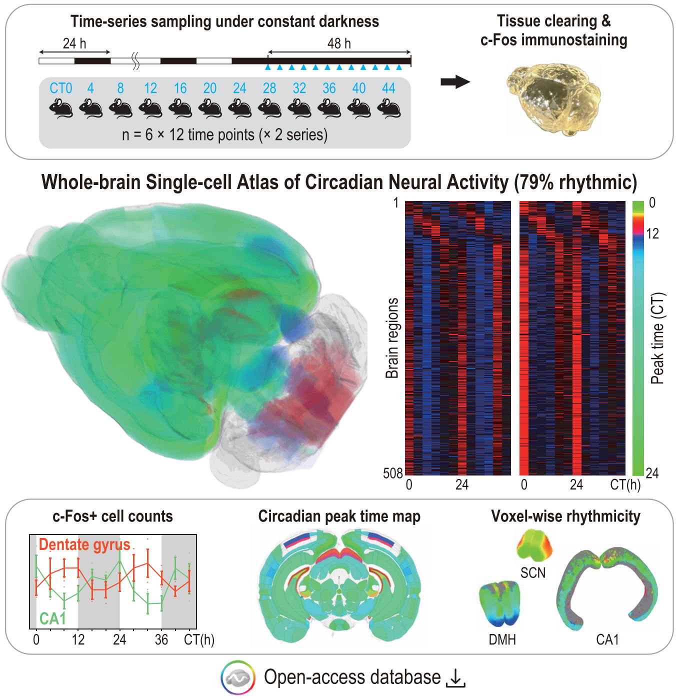

Whole-brain single-cell atlas of circadian neural activity. Time-series sampling of mouse brains under constant darkness, followed by tissue clearing and whole-brain c-Fos immunostaining, enabled the creation of a brainwide atlas of circadian neural activity at single-cell resolution. Analysis of 144 brains revealed significant rhythmicity in 79% of 642 regions, with diverse peak time patterns across brain regions and subregions, all accessible through an open-access database.

Corresponding author: Hiroki R. Ueda (uedah-tky@umin.ac.jp) †These authors contributed equally to this work. **Cite this article as** K. Yamashita *et al.*, *Science* **391**, eaea3381 (2026). **DOI: 10.1126/science.aea3381**

NEUROSCIENCE

A whole-brain single-cell atlas of circadian neural activity in mice

Katsunari Yamashita[1,2,3,4,5]†, Fukuaki L. Kinoshita[1,2,6]†, Shota Y. Yoshida[1,2,4,7], Katsuhiko Matsumoto[1,2], Tomoki T. Mitani[1,2,3,6,8], Hiroshi Fujishima[1,9], Yoichi Minami[2], Eiichi Morii[4], Rikuhiro G. Yamada[1,9], Seiji Okada[5], Hiroki R. Ueda[1,2,3,9]*

The mammalian brain comprises numerous anatomical regions with distinct functions despite their extensive connectivity. How spontaneous neural activity is coordinated across regions over the circadian cycle remains elusive. We used tissue clearing and whole-brain c-Fos immunostaining on 144 mouse brains collected over 2 days under constant darkness. Time-series analysis revealed brainwide circadian rhythmicity at single-cell resolution, with 79% of the 642 anatomically defined regions oscillating in diverse circadian phases that delineate functional specializations. Voxelwise analyses further highlighted distinct subregions, suggesting intricate spatiotemporal coordination within regions. Additionally, brain circadian time could be accurately inferred from global c-Fos patterns using omics-derived prediction methods. This whole-brain circadian atlas enhances our understanding of neural coordination and provides a resource for integrating time-of-day information into functional and pharmacological research.

Neural activity across different brain regions supports a wide range of physiological functions that require coordinated activity patterns both spatially and temporally in the brain. Circadian rhythms are among the most fundamental temporal regulators of neural activity. They regulate many physiological processes, including wakefulness and sleep, metabolism, hormone secretion, and cognitive function. Their disruption is linked to numerous diseases such as metabolic disorders, cardiovascular dysfunction, and neurological conditions (1, 2). Understanding how spontaneous neural activity is coordinated in space and time is essential for characterizing brain functional architecture and for developing targeted interventions such as optimizing drug delivery based on time of day.

Circadian rhythms are generated by cell-autonomous molecular clocks and are orchestrated by the suprachiasmatic nucleus (SCN) in the hypothalamus, the master pacemaker in mammals. The central role and neural complexity of the SCN have been extensively characterized (3, 4). Lesion and transplantation experiments established that the SCN governs circadian rhythms at the organismal level. The SCN is composed of heterogeneous neuronal populations, including arginine vasopressin (AVP)–, vasoactive intestinal peptide (VIP)–, gastrin-releasing peptide (GRP)–, and cholecystokinin-expressing cells, among others, which exhibit different circadian phases and make functionally distinct contributions to SCN coordination (5–8). Although circadian rhythms in the SCN have been well characterized at the molecular and cellular levels, the extent and organization of circadian regulation in other brain regions has not been systematically characterized (9). Previous approaches to studying circadian rhythms in the brain have typically relied on electrophysiological recordings, in situ hybridization, immediate early gene (IEG) labeling, real-time bioluminescent imaging of circadian gene reporters, or calcium imaging. These methods are generally limited to a small number of brain regions and lack spatial continuity, resulting in fragmented and sometimes inconsistent findings (10–12). In addition, accurate assessment of spontaneous neural activity rhythms requires carefully controlled sampling conditions because such activity is easily influenced by subtle environmental variations, which can lead to sampling artifacts. Moreover, the temporal coverage of these studies is often limited, with sparse sampling points, making it difficult to capture the full circadian cycle.

To overcome these limitations, we used tissue clearing and c-Fos immunostaining on whole mouse brains collected in a time series over 2 days with minimal variation in sampling conditions. Tissue clearing renders intact brains transparent while preserving their three-dimensional (3D) structure and allows uniform immunolabeling throughout large tissue volumes (13–15). In addition, c-Fos has been widely used as a marker of neural activation because of its rapid and broad induction across the brain, making it suitable for spatially comprehensive mapping of neural activity (16–19), and in the SCN its expression has long served as an indicator of circadian phase (20–22). This approach enabled unbiased quantification of spontaneous neural activity across the circadian cycle throughout the brain, including anatomically complex and spatially dispersed regions. To examine regional temporal dynamics in the context of global activity, we also established a framework for quantifying the proportion of c-Fos–positive cells in each region relative to the whole brain. All results were compiled into a brainwide 3D atlas of circadian neural activity, which we now provide as an open-access database. This resource provides a foundation for incorporating time-of-day information into studies of brain function, time-dependent drug effects, and neural dynamics associated with disease.

Most brain regions exhibit circadian rhythmicity in c-Fos–positive cell counts

To determine whether circadian rhythms are present across a wide range of brain regions beyond the SCN, we used whole-brain c-Fos immunostaining. Brains from adult male C57BL/6N mice ($n = 6$ per time point) were collected every 4 hours over 2 days (12 time points) under constant darkness (DD) without external light cues. This experiment was repeated in two independent series, yielding a total of 144 samples. We developed a pipeline for whole-brain analysis of c-Fos expression based on the CUBIC (Clear, Unobstructed Brain Imaging Cocktails and Computational analysis) method (14, 23). The brains were cleared and immunostained in 3D and then imaged using light-sheet microscopy. c-Fos–positive cells were automatically detected using a supervised machine learning algorithm trained on multiple spatial and intensity features (figs. S1 to S3 and S4, A and B; see the Materials and methods for details) and mapped onto a standardized whole-brain atlas (Neuron Atlas) (24) to perform regional analysis (Fig. 1A). This atlas is optimized for brain samples processed with the CUBIC-L/R+ protocol and enables fine registration to the Allen Brain Atlas space.

To validate rhythm detection, we first examined the SCN. Time-series visualization of c-Fos expression in the SCN revealed a clear 24-hour rhythmic pattern over two circadian cycles, which was consistently observed in both experimental series (Fig. 1B, fig. S5, and movie S1). Quantitative cell counts confirmed this rhythmicity, with a peak during the subjective day (Fig. 1C). At the whole-brain level, we detected between 0.4 and 3.0 million c-Fos–positive cells per brain across time

---

[1] Laboratory for Synthetic Biology, Center for Biosystems Dynamics Research, RIKEN, Suita, Japan. [2] Department of Systems Pharmacology, Graduate School of Medicine, University of Tokyo, Tokyo, Japan. [3] Department of Systems Biology, Graduate School of Medicine, Osaka University, Suita, Japan. [4] Department of Pathology, Graduate School of Medicine, University of Osaka, Suita, Japan. [5] Department of Orthopaedic Surgery, Graduate School of Medicine, University of Osaka, Suita, Japan. [6] Department of Neurology, Graduate School of Medicine, University of Osaka, Suita, Japan. [7] Department of Pathology, Graduate School of Medicine, University of Tokyo, Tokyo, Japan. [8] Department of Functional Neurology & Neurosurgery, Brain Research Institute, Niigata University, Niigata, Japan. [9] Department of Systems Biology, Institute of Life Science, Kurume University, Kurume, Japan. ***Corresponding author. Email: uedah-tky@umin.ac.jp** †These authors contributed equally to this work.

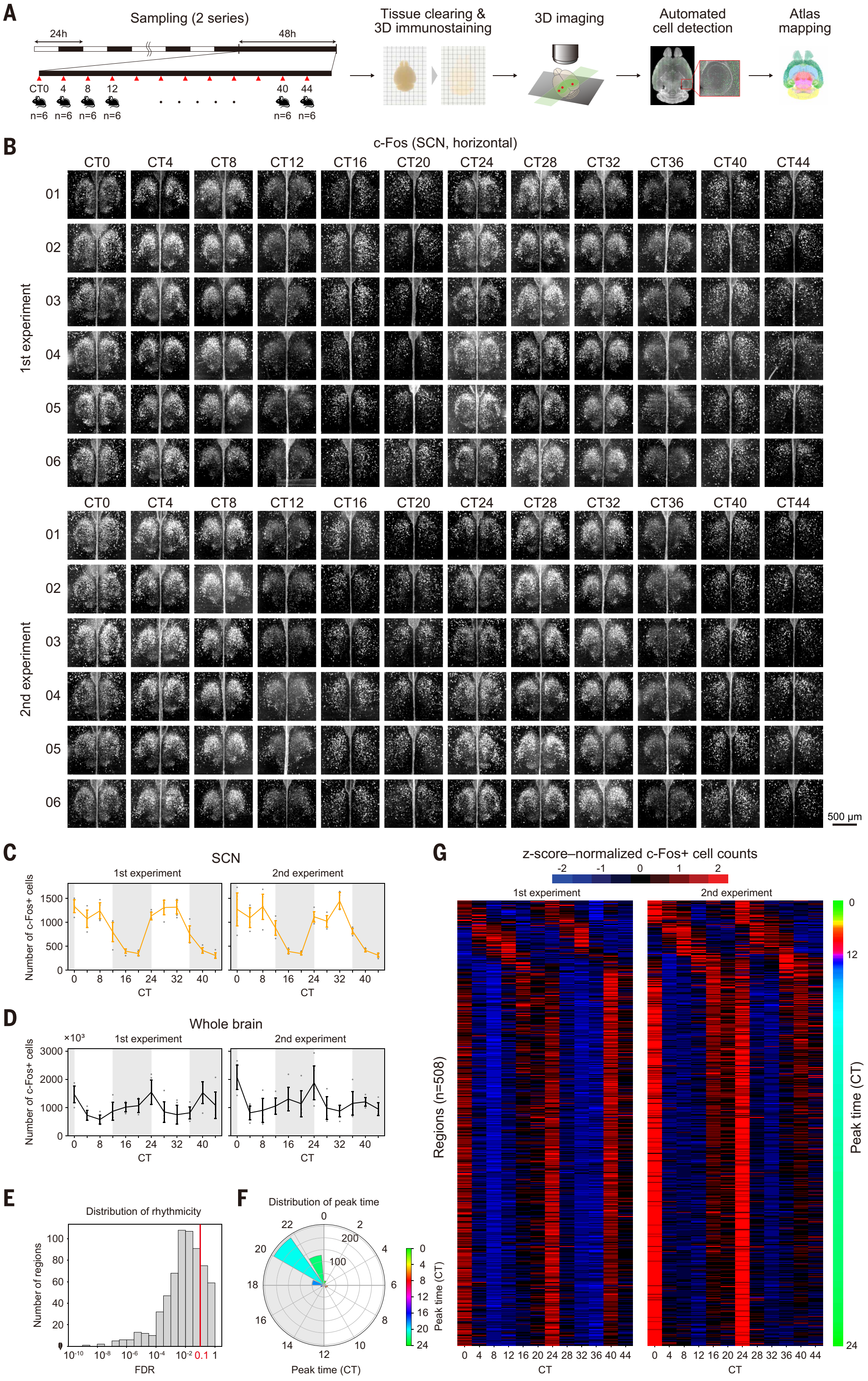

Fig. 1. Temporal dynamics of c-Fos–positive cells in the whole mouse brain. (**A**) Experimental design and workflow. Mouse brains ($n = 6$ per time point) were collected every 4 hours over 2 days under constant darkness. CT starts at subjective dawn (CT0) and continues beyond 24 hours. The brains underwent tissue clearing and 3D immunostaining, 3D imaging using light-sheet microscopy, automated detection of c-Fos–positive cells, and registration to the Neuron Atlas. This pipeline was repeated in two independent series. (**B**) Temporal dynamics of c-Fos expression in the SCN. Horizontal maximum-projection images (500 μm thick) from 144 brains collected at 12 time points in two independent experimental series. Whole-brain signal intensities were median aligned across all 144 brains. Scale bar, 500 μm. (**C**) Temporal dynamics of c-Fos–positive cell counts in the SCN from two independent experiments. Points and error bars represent mean ± SD ($n = 6$ per time point). Time points range from CT0 to CT44 at 4-hour intervals. White and light gray backgrounds denote subjective day and night, respectively. (**D**) Temporal dynamics of total c-Fos–positive cell counts in the whole brain. Data represent mean ± SD across two independent experiments ($n = 6$ per time point). (**E**) Distribution of FDR values for circadian rhythmicity across all brain regions; FDR < 0.1 indicates significant rhythmicity. (**F**) Rose plot showing the distribution of peak times for significantly rhythmic brain regions. Each bar represents the number of regions peaking at that time. The radial axis represents region count, with a maximum of 250. Colors represent peak time. (**G**) Heatmap of z-score–normalized c-Fos–positive cell counts across 508 rhythmic brain regions. Rows represent brain regions ordered by peak time. Colors represent normalized cell count (red: high, blue: low).

points, with the highest counts observed around the transition from the subjective night to day (Fig. 1D).

To efficiently evaluate circadian rhythmicity, we applied an analytic cosinor test developed for high-throughput analysis (see the Materials and methods). To identify brain regions with consistent circadian rhythmicity, we concatenated the two experimental courses into a continuous 4-day dataset, which provided the most coherent results. Of the 642 annotated brain regions, 508 (79%) showed significant rhythmicity at a false discovery rate (FDR) < 0.1 (Fig. 1E and table S4). This result was independently supported by JTK_CYCLE analysis (*25*), which identified 549 rhythmic regions (FDR < 0.05), with 500 overlapping between the two methods (fig. S6).

We next analyzed the temporal distribution of peak times in the rhythmic regions. Although the SCN peaked around circadian time (CT) 5.3, a large proportion of regions peaked during the late subjective night (CT20 to CT24), particularly around CT20 to CT22, corresponding to the late active phase in mice (Fig. 1F). To illustrate temporal patterns across brain regions, we generated heatmaps of z-score–normalized c-Fos–positive cell counts ordered by circadian peak time (Fig. 1G). This representation highlighted the consistent clustering of peak times during the late subjective night across both experiments, demonstrating high reproducibility.

Spatial mapping of peak times reveals characteristic circadian rhythms across brain regions

Some brain regions exhibited peak times that diverged from the dominant pattern, as observed in Fig. 1G. To investigate the spatial distribution of rhythmicity across brain regions, we mapped regional peak times of c-Fos–positive cell counts onto the Neuron Atlas (Fig. 2A; for rhythmicity analysis results, see table S4). This spatial map demonstrated that most brain regions peaked during the late subjective night (CT20 to CT24), whereas some regions, including parts of the isocortex, hippocampus, thalamus, and hypothalamus, showed peak times during the subjective day (CT0 to CT12; inactive phase). In posterior brain areas, including parts of the hindbrain and cerebellum, several regions peaked during the early subjective night (CT12 to CT18) or late subjective day (CT6 to CT12).

To examine peak times across brain regions in more detail, we arranged the annotated regions by 10 major brain divisions based on the hierarchical anatomical divisions of the Allen Brain Atlas (CCFv3) (*26*) and visualized their peak times using grid plots (Fig. 2B). Rose plots summarized the distribution of peak times within each division (Fig. 2C).

Within the isocortex, the auditory (AUD) areas tended to peak earlier (CT18.5 to CT21.3) than other cortical regions, which mostly peaked between CT20 and CT24 (Fig. 2B and table S4). The primary visual area, layer 4 (VISp4) peaked during the subjective day (CT8.8), standing out among cortical regions. In the hippocampal formation, the dentate gyrus, granule cell layer (DG-sg), and the entorhinal area, medial part, dorsal zone, layer 5 (ENTm5), peaked around the midsubjective day (CT6.9 and CT5.7, respectively). In the thalamus, most regions peaked around CT22 to CT24 (Fig. 2C), whereas the dorsal part of the lateral geniculate complex (LGd), which is involved in visual processing, peaked during the midsubjective day (CT6 to CT8). In the hypothalamus, several regions showed distinct peak times, such as the ventrolateral preoptic area (VLPO) during the midsubjective day (CT6.5), the supraoptic nucleus (SO) around the transition from day to night (CT12.4), and the paraventricular nucleus (PVH) during the midsubjective night (CT17.7). In the midbrain, auditory-related regions such as the inferior colliculus–central nucleus (ICc), dorsal nucleus (ICd), and external nucleus (ICe) peaked during CT17 to CT18, whereas visual-related regions such as the superior colliculus–optic layer (SCop), superficial gray layer (SCsg), and zonal layer (SCzo) peaked around CT6 to CT10, showing an antiphase. In the hindbrain, although relatively fewer regions showed rhythmicity, they displayed a broad distribution of peak times. In the cerebellum, regions with rhythmicity consistently peaked during the late subjective day (CT6 to CT10), although the number of c-Fos–positive cells detected in these regions was limited. Lastly, regions in the olfactory areas, the cortical subplate, and the cerebral nuclei predominantly peaked around CT20 to CT22.

Similar circadian rhythms are observed in brain regions with related physiological functions

We categorized brain regions based on their physiological functions and evaluated the circadian patterns of c-Fos–positive cell counts within each category. This approach allowed us to identify characteristic trends in rhythmicity associated with specific functional groups.

Well-established wake-related brain regions peaked during the late subjective night, corresponding to the active phase of nocturnal animals. These include the tuberomammillary nucleus, ventral part (TMv), the dorsal nucleus raphe (DR), and the lateral hypothalamic area (LHA) (CT20.2, CT20.9, and CT21.6, respectively), all of which secrete wake-promoting neurotransmitters such as histamine, serotonin, and orexin, respectively (Fig. 3A and fig. S7A) (*27*). The paraventricular nucleus of the thalamus (PVT), a limbic-hypothalamic relay activated during wakefulness (*28*), also peaked during the late subjective night (CT22.9).

Rapid eye movement (REM) sleep–related regions also showed peak times during the late subjective night. These include the sublaterodorsal nucleus (SLD), the pedunculopontine tegmental nucleus (PPT), and the laterodorsal tegmental nucleus (LDT) (CT20.5, CT23.8, and CT23.2, respectively) (Fig. 3B and fig. S7B). Although these regions are important in REM sleep regulation (*29*), given the limited temporal resolution of c-Fos, the observed peak times should not be taken as evidence for circadian modulation of the fast dynamics of REM sleep.

Non–rapid eye movement (NREM) sleep–related regions peaked during the subjective day (inactive phase), although their peak times were not consistent (Fig. 3C and fig. S7C). The VLPO, a sleep-promoting center that inhibits wake-promoting regions (*29*, *30*), peaked around the midsubjective day (CT6.5). The medial preoptic area (MPO), which coordinates sleep with thermoregulation, and the reticular nucleus of the thalamus (RT), which regulates thalamocortical rhythms including delta waves and sleep spindles, peaked earlier (CT1.9 and CT1.6, respectively) (*31*).

Memory-related regions displayed divergent peak times. CA1 and CA3, which support memory retrieval through information integration and pattern completion, respectively (*32*), peaked during the late subjective night (CT21.9 and CT21.7, respectively). By contrast, the DG-sg, which supports memory encoding through pattern separation (*33*), peaked around the opposite CT (CT6.9). The ENTm5, a key relay connecting the hippocampus to the neocortex (*34*), showed a peak around CT5.7, close to that of the DG (Fig. 3D and fig. S8A).

Regions associated with the reward system (*35*), including the ventral tegmental area (VTA), the nucleus accumbens (ACB), the lateral habenula (LH), and the basolateral amygdalar nucleus, anterior part (BLAa), peaked during the late subjective night (CT21.5, CT21.1, CT20.8, and CT22.2, respectively) (Fig. 3E and fig. S8B) . These peak times are consistent with increased reward-seeking behavior during the active phase of nocturnal animals (*36*).

Regions associated with visual functions and photic inputs, including the nucleus of the optic tract (NOT), the olivary pretectal nucleus (OP) (*37*), the SCsg, the dorsal part of the lateral geniculate complex, core (LGd-co), and the VISp4, peaked during the subjective day (CT6.3, CT6.4, CT7.3, CT7.9, and CT8.8, respectively) (Fig. 3F and fig. S8C). These daytime peaks suggest robust circadian rhythmicity independent of external light cues, as is also observed in the SCN (Fig. 1C). Among the auditory regions, the primary auditory cortex, layer 4 (AUDp4), and the ICc, a midbrain hub for auditory processing (*38*), both peaked during the midsubjective night (CT19.6 and CT17.1, respectively) (Fig. 3G and fig. S8D). These peak times contrast with those of visual regions.

Regions associated with voluntary motor function, including the primary motor area, layer 2/3 (MOp2/3), the secondary motor area, layer 2/3 (MOs2/3), the globus pallidus, internal segment (GPi), a major output nucleus of the basal ganglia (*39*), and the substantia nigra, compact part (SNc), a major source of dopamine input to the striatum (*40*), peaked during the late subjective night (CT22.0, CT21.6, CT21.3, and CT22.0, respectively) (Fig. 3H and fig. S9A). By contrast, regions associated with involuntary motor functions, such as vestibular control, including the nodulus (NOD) (*41*), the vestibulocerebellar nucleus, (VeCB) (*42*), and the medial vestibular nucleus (MV) (*43*), peaked during the

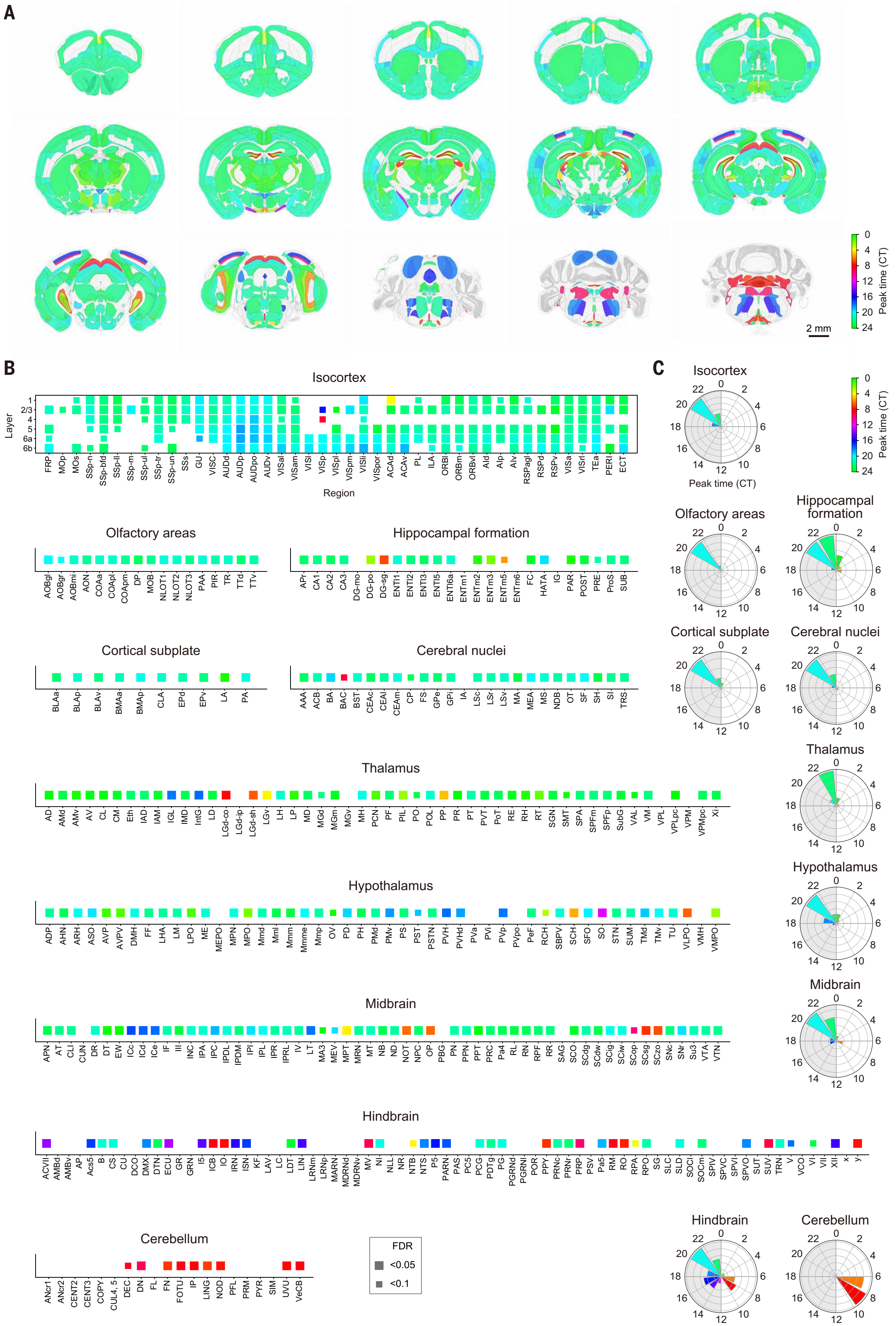

Fig. 2. Brainwide distribution of circadian peak times of c-Fos–positive cell counts. (**A**) Coronal sections at 800-μm intervals showing peak times of rhythmic regions overlaid on inverted nuclear staining images of the Neuron Atlas with annotation outlines. Colors represent peak time. Scale bar, 2 mm. (**B**) Grid plots of peak times of

566 annotated regions (of 642 total regions, excluding fiber tracts and ventricular systems), grouped into 10 major brain divisions: isocortex, olfactory areas, hippocampal formation, cortical subplate, cerebral nuclei, thalamus, hypothalamus, midbrain, hindbrain, and cerebellum. Full-size squares indicate regions with FDR < 0.05; half-size squares indicate 0.05 ≤ FDR < 0.1. Region abbreviations are listed in table S5. (**C**) Rose plots showing the distribution of peak times for significantly rhythmic regions (FDR < 0.1) across the 10 major brain divisions. Each bar represents the number of regions within a 2-hour bin. Radial scales vary by division; one grid unit corresponds to 20, 3, 2, 2, 3, 5, 4, 5, 2, and 1 regions, respectively.

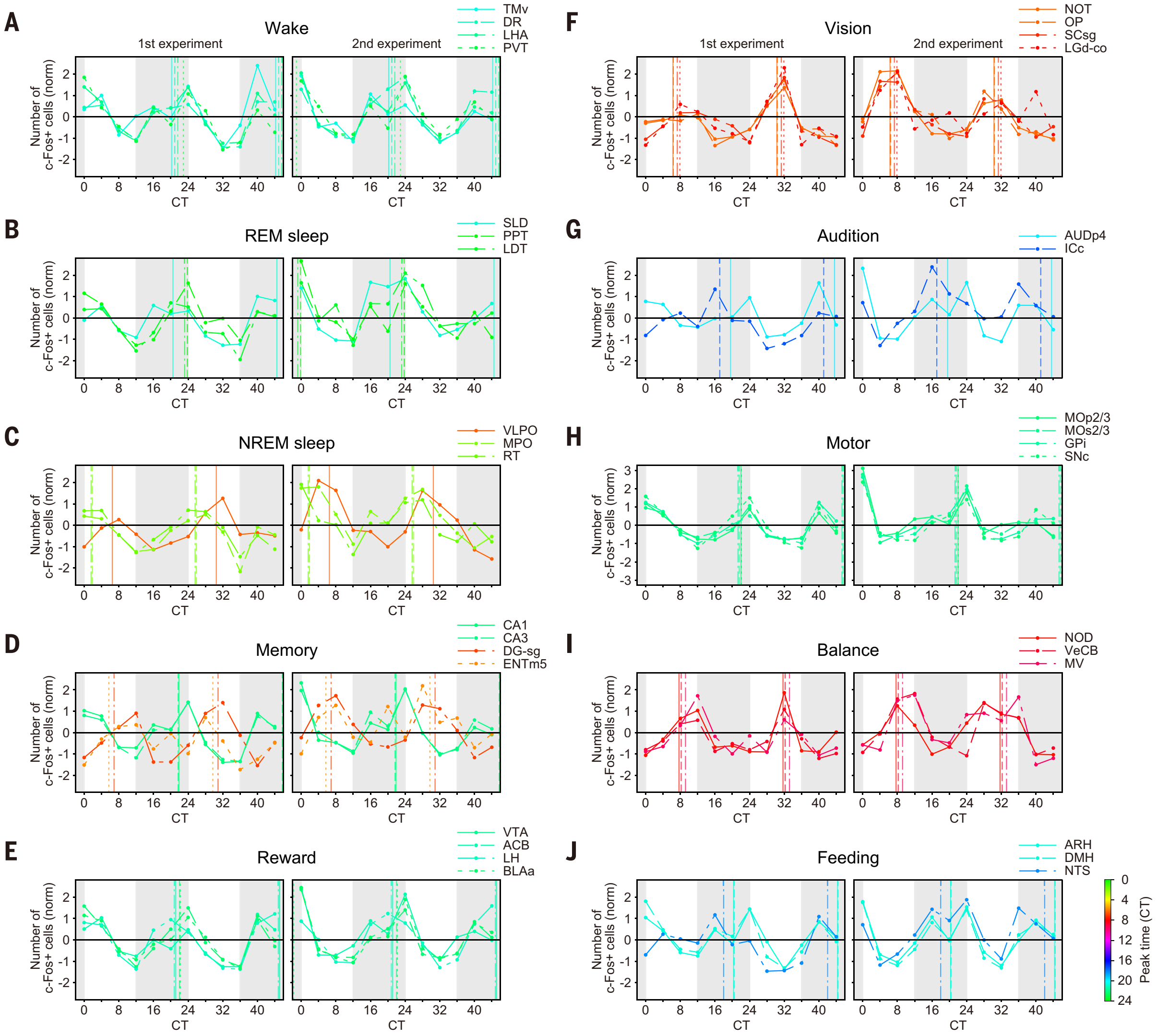

Fig. 3. Temporal dynamics of c-Fos–positive cell counts in brain regions with related physiological functions. (**A** to **J**) Line plots of z-score–normalized c-Fos–positive cell counts for representative rhythmic regions in 10 functional categories: wake, REM sleep, NREM sleep, memory, reward, vision, audition, motor, balance, and feeding. Line color represents the peak time of each region. Vertical lines indicate the peak time of each region calculated over the first and second experiments. Line styles (solid and dashed) differentiate regions within each category. White and light gray backgrounds denote subjective day and night, respectively. Raw cell counts and error bars for each region are shown in figs. S7 to S9. TMv, tuberomammillary nucleus, ventral part; DR, dorsal nucleus raphe; VTA, ventral tegmental area; LHA, lateral hypothalamic area; SLD, sublaterodorsal nucleus; PPT, pedunculopontine tegmental nucleus; LDT, laterodorsal tegmental nucleus; VLPO, ventrolateral preoptic nucleus; MPO, medial preoptic area; RT, reticular nucleus of the thalamus; CA1, field CA1; CA3, field CA3; DG-sg, dentate gyrus, supragranular layer; ENTm5, entorhinal area, medial part, layer 5; ACB, nucleus accumbens; SNc, substantia nigra, compact part; LH, lateral habenula; BLAa, basolateral amygdalar nucleus, anterior part; NOT, nucleus of the optic tract; OP, olivary pretectal nucleus; SCsg, superior colliculus, superficial gray layer; LGd-co, dorsal part of the lateral geniculate complex, core; AUDp4, primary auditory area, layer 4; ICc, inferior colliculus, central nucleus; MOp2/3, primary motor area, layer 2/3; MOs2/3, secondary motor area, layer 2/3; GPi, globus pallidus, internal segment; NOD, nodulus; VeCB, vestibulocerebellar nucleus; MV, medial vestibular nucleus; ARH, arcuate hypothalamic nucleus; DMH, dorsomedial nucleus of the hypothalamus; NTS, nucleus of the solitary tract.

late subjective day (CT7.7, CT8.2, and CT9.2, respectively) (Fig. 3I and fig. S9B).

Feeding-related regions (*44*), including the arcuate hypothalamic nucleus (ARH), the dorsomedial nucleus of the hypothalamus (DMH), and the nucleus of the solitary tract (NTS), peaked around the mid-subjective night (CT20.3, CT20.4, and CT18.0, respectively) (Fig. 3J and fig. S9C). The SO, which plays a central role in water balance through vasopressin secretion (*45*), peaked near the onset of the subjective night (CT12.4) (fig. S9D).

Regions with similar physiological functions often exhibited common peak times. We also observed that functionally similar regions, such as hippocampal memory-related regions, sometimes displayed distinct circadian peak times. This prompted us to explore whether such diversity could also be present within individual brain regions, motivating a finer-resolution analysis.

Voxelwise analysis reveals distinct peak times within brain regions

To investigate circadian rhythms of c-Fos–positive cell counts at higher spatial resolution, we performed voxelwise analysis at a 20-μm voxel scale. To ensure robust analysis across multiple brain images, we applied a convolution step: the c-Fos–positive cell count for each voxel was calculated from the total number of cells within a surrounding 160-μm cubic volume (fig. S10, A and B). After this smoothing step, rhythmicity was evaluated voxelwise throughout the entire brain using the analytic cosinor test that we developed. This approach enabled efficient rhythmicity analysis of >100 million voxels per brain.

The SCN, which peaked around CT5.3 when analyzed as a whole (Fig. 1C), exhibited various peak times at the voxel level, ranging from earlier peak times in an anterior dorsomedial area (approximately CT2 to CT4) to later in a ventrolateral area (approximately CT4 to CT8) (Fig. 4, A and B). The classical "shell" region included both of these areas, whereas the "core" contains part of the later-peak time area (CT4 to CT8) along with nonrhythmic voxels (*7*). The regions surrounding the SCN showed a wide variety of peak times. The subparaventricular zone (SBPV), just dorsal to the SCN and relaying circadian signals to autonomic centers (*46*), showed an almost opposite peak time (CT15 to CT22; fig. S10C). The DMH, which peaked around CT20.4 when analyzed as a whole (fig. S9C), also exhibited temporal heterogeneity, with an earlier peak time in its posterior ventral area (approximately CT14 to CT20). In the entorhinal cortex (ENT), the medial area peaked around CT8, whereas the lateral area peaked around CT20 to CT24. In CA1, a gradual peak time shift was observed along the dorsoventral axis, with the ventral area peaking earlier than the dorsal area (approximately CT18 to CT2).

In contrast to the subregional diversity described above, some brain regions exhibited coherent circadian peaks that were well aligned with anatomical boundaries, as revealed by voxelwise analysis (Fig. 4C). In the isocortex, rhythmic voxels with daytime peaks were tightly confined to the narrow layer of the VISp4 (approximately CT6 to CT12), whereas the primary auditory cortex (AUDp) showed a laminar distribution with a distinctive peak time in layer 5 (approximately CT18 to CT21), although its boundary was relatively broad. In the midbrain, the superior colliculus, sensory related (SCs), comprising the SCop, SCsg, and SCzo, peaked around CT5 to CT10. These peak times were distinct from those of the surrounding regions, delineating a characteristic layered structure resembling paired domes in horizontal or coronal views. By contrast, the inferior colliculus (IC), comprising the ICc, ICd, and ICe, showed an opposite peak time around CT15 to CT21, although rhythmic voxels were relatively sparse and unevenly distributed (Figs. 4C and 2B).

The diversity of relative peak times enables prediction of brain CT in single samples

Rhythmicity analysis based on regional c-Fos–positive cell counts revealed that most brain regions peaked around CT20 to CT24, broadly aligned with the temporal fluctuation of whole-brain c-Fos–positive cell counts (Fig. 1D). This led us to hypothesize that the temporal dynamics of brain regions, viewed relative to global brain activity, might reveal region groups that contribute most prominently at different CT points. We thus calculated the cell count ratio for each region by dividing the c-Fos–positive cell counts in that region by the total c-Fos–positive cell counts in the entire brain at each time point (Fig. 5A). Of the 642 annotated regions, 393 showed significant circadian rhythmicity in cell count ratio (FDR < 0.1) (table S7). Compared with raw counts, the distribution of peak times based on cell count ratios (referred to as relative peak times) was more evenly spread across the circadian cycle (Fig. 5B). Here, relative peak time indicates the CT point when a region shows its highest activity relative to the entire brain.

To illustrate this diversity, the regions showing rhythmicity in cell count ratio were grouped into six time windows: dawn (CT22 to CT2), morning (CT2 to CT6), afternoon (CT6 to CT10), evening (CT10 to CT14), early night (CT14 to CT18), and late night (CT18 to CT22) (Fig. 5C). Each time window showed a distinct spatial configuration of peaking regions, forming a structured circadian pattern across the brain. For a more detailed view, the relative peak time distributions of these regions were organized by major brain divisions (fig. S11). The isocortex showed a wide range of relative peak times, with a tendency to peak during the late subjective night (active phase). The thalamus peaked predominantly during the early subjective day (inactive phase). The hippocampal formation, hypothalamus, hindbrain, and cerebellum peaked mainly around the late subjective day. The midbrain showed a distribution of peak times with two tendencies, one in the late subjective day and another in the late subjective night. The olfactory areas, cortical subplate, and cerebral nuclei tended to peak during the late subjective night (fig. S11C).

The broad distribution of relative peak times suggested that a profile of regional c-Fos cell count ratios at a single time point could carry sufficient information to infer CT (*47*). We therefore retrospectively estimated the CT of individual brain samples using two analytical approaches: a molecular timetable method that we previously developed (*48*, *49*) and an unsupervised algorithm known as cyclic ordering by periodic structure (CYCLOPS) (*50*).

The molecular timetable method was originally designed to estimate circadian phase from transcriptomic data by identifying and leveraging time-indicating genes. In the present study, although the relative peak times of brain regions were broadly distributed, they remained somewhat skewed compared with transcriptome-derived phase indicators (fig. S12A). To address this, we filtered regions within each peak time window based on the lowest FDR values, yielding 216 regions with well-distributed peak times (fig. S12B and see the Materials and methods). For each sampling time point of each experimental day, we visualized the distribution of z-score–normalized cell count ratios across regions, ordered by their relative peak times. The resulting profiles formed sinusoidal curves aligned with CT, enabling us to construct a brain circadian timetable (Fig. 5D). Using a leave-one-out cross-validation approach, we fitted each sample to this reference curve and inferred its sampling time with high accuracy (mean absolute error: 1.44 ± 0.24 hours; Fig. 5E and fig. S12, C to E). This approach demonstrated high sensitivity and specificity even with fewer input regions (fig. S12, F to H). Sensitivity and specificity showed only minor variation across CTs (fig. S12, I and J).

We further applied CYCLOPS, a previously developed unsupervised method for reconstructing circadian order based on latent periodic structure (*50*). With appropriate parameter settings, such as the number of regions used to obtain characteristic patterns, CYCLOPS also predicted brain CT with comparable accuracy (mean error: 1.47 ± 0.21 hours; fig. S13).

An open-access database enables multiperspective circadian rhythmicity analysis of the whole brain

In this study, we constructed a whole-brain atlas of circadian rhythmicity based on c-Fos–positive cell counts or cell count ratios at both regional and voxel levels, covering all brain regions.We now provide a freely accessible database at https://circadian.cfosdb.systems-based-medicine.org/database, allowing users to explore the data from multiple perspectives (Fig. 6A). Brain regions can be selected in several ways: through a 3D/2D slice viewer, the anatomical tree based on the Allen Mouse Brain Atlas, or a rhythmicity-based query. Output options include (i) line plots of c-Fos–positive cell counts in selected regions (Fig. 6B), (ii) time-series images showing c-Fos expression across 24 time points concatenated from two time courses in independent experimental

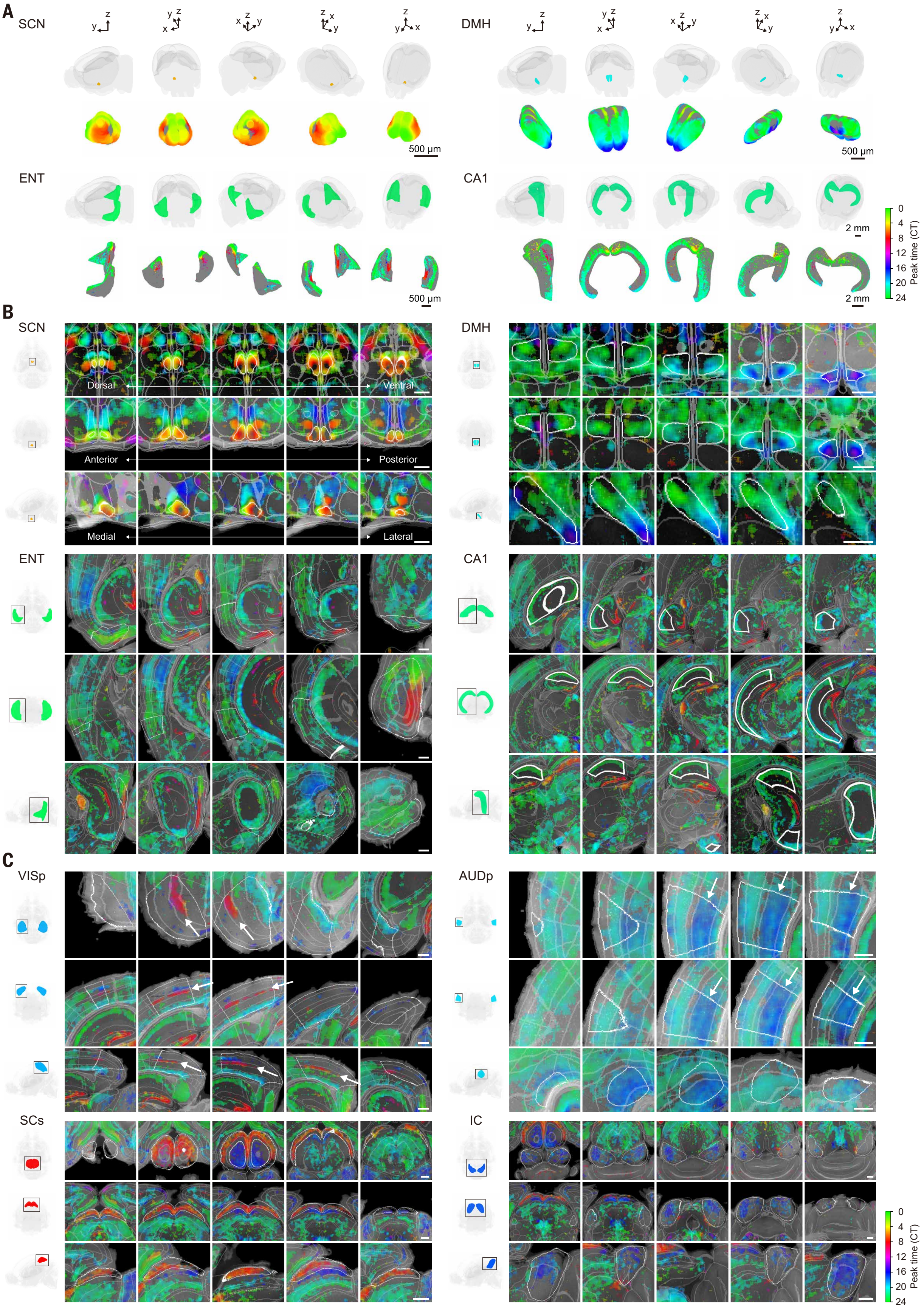

Fig. 4. Voxelwise circadian rhythmicity analysis of c-Fos–positive cell counts in representative brain regions. (**A**) Circadian peak times in 3D views of representative brain regions. Upper panels show anatomical location in the whole brain, colored by region-level peak time. Scale bar, 2 mm. Lower panels show 3D maps of voxelwise peak times at

20-µm voxel resolution. Colors represent peak time; gray voxels indicate voxels without significant rhythmicity (FDR ≥ 0.1). Scale bars, 500 µm (SCN, DMH, ENT), 2 mm (CA1). (**B** and **C**) Circadian peak times in 2D views of representative brain regions. For each region, the left column shows its anatomical location in the whole brain. The right columns show five projection views of voxelwise peak times in three orientations (horizontal, coronal, and sagittal from top to bottom). Each projection corresponds to one of five equally spaced partitions along the respective axis. Sagittal views generally show the right hemisphere, except for SCs and IC, where bilateral projections are displayed. Colors represent peak time; transparency reflects rhythmicity (lower FDR values appear more opaque). c-Fos immunostaining images are shown underneath for anatomical reference. Opaque and translucent white outlines denote the region of interest and its surrounding regions, respectively. White arrows indicate layer 4 of VISp (left) and layer 5 of AUDp (right). Scale bars, 500 µm. SCN, suprachiasmatic nucleus; DMH, dorsomedial nucleus of the hypothalamus; ENT, entorhinal area; CA1, field CA1; SCs, superior colliculus, sensory related; IC, Inferior colliculus; VISp, primary visual area; AUDp, primary auditory area.

series (Fig. 6C), and (iii) time-series movies and voxelwise visualizations of peak times (Fig. 6D, fig. S14, and movie S2). These outputs facilitate comparisons across hemispheres and spatial planes (coronal, horizontal, and sagittal). The database also provides whole-brain slice views of rhythmicity analysis results, where peak times are displayed in color based on either cell counts or cell count ratios at the regional or voxel level (fig. S15). In addition to predefined anatomical regions, users can define regions of interest (ROIs) by creating binary masks using external image analysis software and upload them for rhythmicity analysis (Fig. 6A). As a demonstration, we manually defined regions adjacent to the dorsal and medial borders of the VLPO called the extended dorsal and medial VLPO (edVLPO and emVLPO, respectively; Fig. 6E) (*51*). Rhythmicity analysis of these user-defined areas revealed a peak time around CT5.3, slightly earlier than the originally defined VLPO (CT6.5; Fig. 6F and fig. S7C).

Discussion

3D mapping of circadian neural activity confirms spatially coherent rhythms in the SCN

The SCN illustrated how 3D staining enables precise global mapping of circadian neural activity. Our cell detection and rhythmicity analysis revealed a clear circadian rhythm in the SCN, with a peak around CT5.3 when analyzed as a whole. Voxelwise analysis further revealed a gradual shift in peak times from the anterior dorsomedial to the ventrolateral area, spanning approximately CT2 to CT8. This timing is consistent with previously reported c-Fos expression and electrophysiological findings (*20*, *21*, *52*), supporting the validity of our atlas and analysis pipeline.

The SCN core is enriched in VIP and GRP neurons that receive direct retinal input and drive light entrainment, whereas its shell predominantly contains AVP neurons that support interneuronal coupling and sustain circadian rhythmicity (*3*, *53*). Core and shell exhibit distinct circadian phases, and some cell populations within the core may lack detectable rhythmicity (*54*). Beyond this binary structure, a series of studies using real-time PER2::luciferase bioluminescence imaging (*5*, *54*, *55*) and calcium imaging (*56*, *57*) have revealed a continuous spatial gradient of circadian peak times across the SCN. In our study, voxelwise analysis demonstrated a continuous gradient of activity peak time across its anatomical subregions, a pattern consistent with these previous studies. Recent single-cell and spatial transcriptomic studies have provided a molecular atlas of the SCN and revealed that distinct neuronal subtypes are spatially intermixed and exhibit phase-shifted rhythms (*7*, *8*). The peak time gradient in our study may reflect, at least in part, this spatial distribution of neuronal subtypes and the underlying cellular heterogeneity in circadian peak time.

Brain regions regulating the sleep-wake cycle exhibit distinct circadian activity patterns

Beyond the SCN, the regulation of sleep and wakefulness involves a distributed network of subcortical regions that interact with circadian and homeostatic processes (*58*, *59*). Despite their known functional roles, their circadian dynamics have not been assessed comprehensively at the whole-brain level. In our study, we addressed this gap and revealed a clear temporal contrast between wake- and sleep-related regions.

Wake-promoting regions, such as the TMv, DR, LHA, PVT, and magnocellular nucleus (MA) in the basal forebrain, peaked during the late active phase (CT20.2 to CT22.9), consistent with previous reports showing elevated neural activity in these regions during wakefulness (*28*, *60*–*63*). This timing corresponds to the wake maintenance zone, originally described in humans, when circadian wake drive counteracts increasing sleep pressure (*64*). The delayed peak times in these regions suggest that they may be more involved in sustaining wakefulness or supporting ongoing wake-related processes, rather than simply initiating the sleep-wake transition. The PVH peaked earlier (CT17.7) than other wake-promoting regions, consistent with its proposed role in initiating arousal through corticotropin-releasing factor signaling and orexin activation (fig. S7A) (*65*). By contrast, the locus coeruleus (LC) did not show significant rhythmicity, which may reflect an insufficient number of c-Fos–positive cells for reliable detection of circadian rhythmicity. However, voxelwise analysis revealed a rhythmic subregion within the LC (fig. S10C). The Kölliker-Fuse nucleus, a region within the parabrachial nucleus (PB), also did not show significant rhythmicity, possibly reflecting functional heterogeneity within the PB complex, which is known to contribute to wake maintenance (*66*).

REM sleep–related regions also peaked during the late subjective night. The SLD, essential for REM induction and muscle atonia (*29*), peaked around CT20.5. The PPT and LDT, traditionally regarded as REM generators but also active during wakefulness (*30*), peaked around CT23.2 to CT23.8. These timings suggest that their circadian activity does not directly reflect REM dynamics, but rather may be associated with other physiological processes, including wakefulness. By contrast, NREM sleep–related regions peaked during the subjective day, especially the VLPO, which showed a clear rhythm with a peak around CT6.5. The MPO and RT peaked earlier (CT1.6 to CT1.9), possibly reflecting roles in the early inactive phase, which should be considered in studies of thermoregulation and sleep-related brain oscillations. Nevertheless, our voxelwise analysis suggests that their oscillatory activity is subregion dependent.

The hippocampal memory system exhibits distinct circadian activity patterns across regions and subregions

The hippocampal memory system comprises anatomically and functionally distinct regions (*67*). In our study, these regions exhibited distinct circadian peak times. CA1 and CA3 peaked around CT21.7 to CT21.9, consistent with previous reports of elevated activity during the active phase (*68*). By contrast, the DG peaked around CT6.9 during the inactive phase, nearly in antiphase to the CA regions. This aligns with reports that the DG and CA regions play distinct roles depending on behavioral state (*69*, *70*). Several studies report higher activation of the DG during NREM and REM sleep (*10*, *12*, *71*), whereas others observed increased activity during wakefulness (*11*, *72*). This inconsistency may reflect differences in behavioral state, measurement techniques, or the anatomical complexity of the DG. Voxelwise analysis further revealed subregional variation in circadian peak times. CA1 showed a gradual peak time shift along the dorsoventral axis, possibly reflecting continuous changes in gene expression patterns and cell types (*73*, *74*). Previous studies have also reported day-night variation along the anterior-posterior axis of the dorsal hippocampus (*75*), and in our dataset spatially limited peak

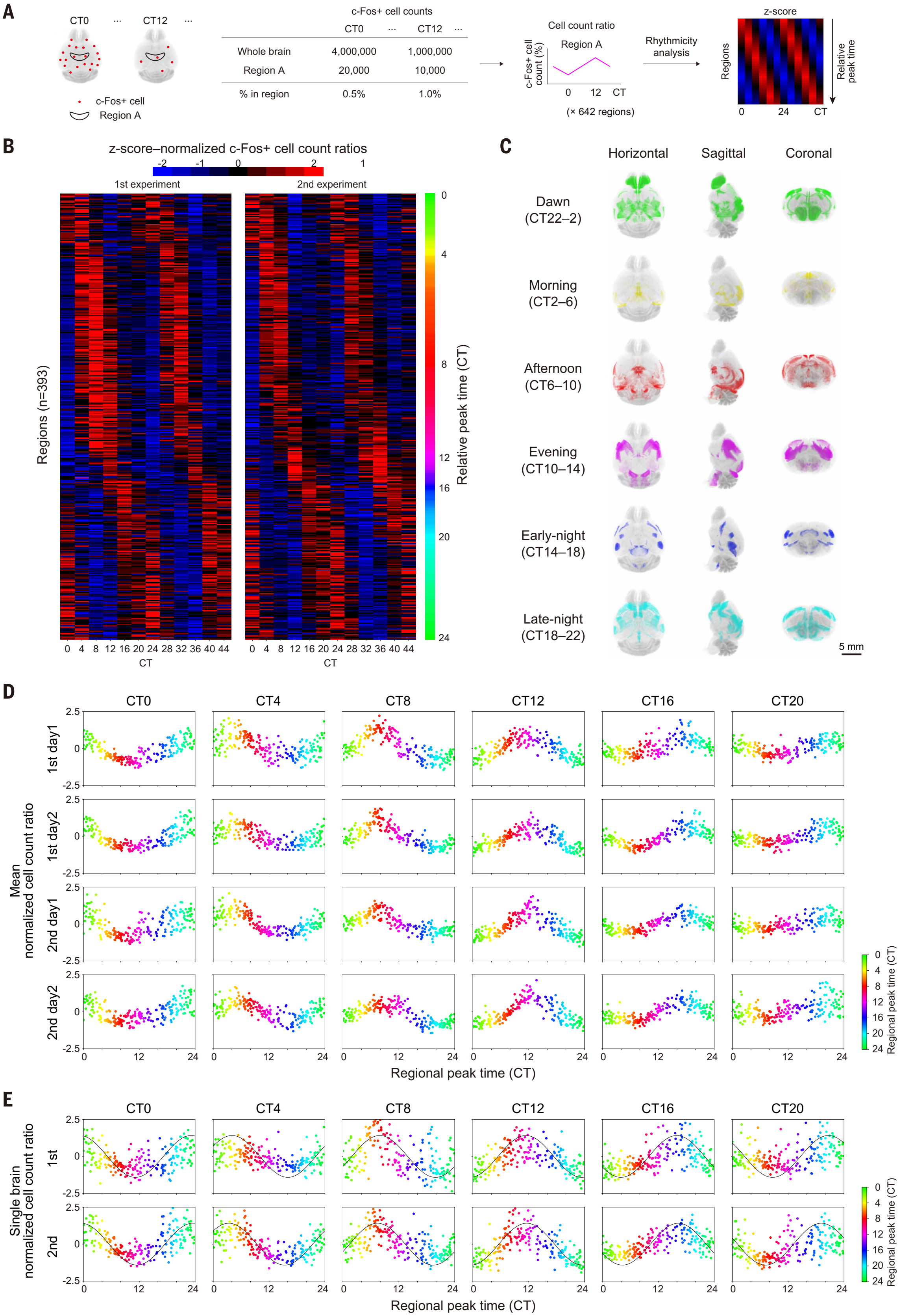

Fig. 5. Brain CT prediction based on the pattern of regional c-Fos–positive cell count ratios. (**A**) Schematic of cell count ratio calculation and rhythmicity analysis. For each brain region and time point, the number of c-Fos–positive cells was divided by the whole-brain total at that time point to compute the cell count ratio. Rhythmicity was evaluated using the analytic cosinor test. A conceptual heatmap of z-score–normalized ratios is shown to illustrate relative peak time distributions. (**B**) Heatmap of z-score–normalized c-Fos–positive cell count ratios across 395 brain regions showing significant rhythmicity in cell count ratio. Rows represent brain regions ordered by relative peak time. Colors

represent normalized cell count ratio (red: high, blue: low). (**C**) 3D visualization of the brain regions shown in (B) grouped by relative peak time. Regions are classified into six time windows. Each group is shown in three anatomical views: horizontal, sagittal, and coronal. Regions are color coded according to the central time of each window. Scale bar, 5 mm. (**D**) Temporal profiles of normalized cell count ratios in 216 regions showing significant rhythmicity in cell count ratio. Regions were filtered within each peak time window based on the lowest FDR values. Ratios were z-score normalized per region across all 144 samples. Samples were grouped by experimental series and day (first experiment: day 1 and day 2; second experiment: day 1 and day 2). Each curve shows the mean ratio across six samples per time point. Line color represents the relative peak time of each region (color code shown at right). (**E**) Brain CT prediction based on cell count ratio profiles. For each sample, brain CT was predicted using the timetable method trained on the remaining 143 samples. Cell count ratios were z-score normalized per region using only the training set. Predicted brain CT was defined as the peak of the best-fit cosine curve (black line). Representative predictions are shown for each time point in both experimental series (CT23.2, CT4.0, CT7.9, CT11.4, CT15.9, and CT20.6 in the first experiment; CT23.5, CT3.4, CT7.4, CT11.6, CT16.3, and CT19.1 in the second experiment).

time differences were observed (Fig. 4A). In the DG, daytime peaks were spatially aligned with the granule cell layer (fig. S10C). The ENT also exhibited spatial variation in peak time; notably, part of the medial area peaked during the light phase, whereas the lateral area peaked during the late subjective night. This may reflect the functional division of the ENT, where the medial part encodes spatial information (*76*) and the lateral part processes nonspatial cues (*77*), with the latter showing increased activity during the active phase (*72*). These findings underscore the importance of considering circadian timing in studies of hippocampal memory–related functions, which are subject to time-of-day-dependent modulation of plasticity and excitability.

Brain regions supporting diverse behavioral functions show distinct circadian activity patterns

Circadian clocks provide an evolutionary advantage by enabling organisms to anticipate predictable daily environmental changes and temporally optimize physiological processes, including reward, motor control, sensory processing, and feeding. Disruption of the molecular circadian clock in the VTA, a central hub of the dopaminergic system, impairs reward-related behavior (*78*). However, the circadian organization of neural activity across the broader reward system has not been comprehensively examined. In our study, multiple reward-related brain regions, such as the ACB, LH, and BLAa, peaked during the late subjective night, in phase with the VTA. These peak times align with behavioral studies showing increased sensitivity to rewards such as food or social stimuli during the active phase (*36*).

Similarly, brain regions involved in voluntary motor control, such as the MOp2/3, MOs2/3, GPi, and SNc, peaked during the late subjective night. By contrast, cerebellar and medullary regions associated with involuntary motor control, such as balance, posture, and eye movement, tended to peak during the inactive phase. Although the cerebellum contributes to refining voluntary movement, its activity under DD conditions may reflect internally generated processes, consistent with reports of state-dependent cerebellar activity during sleep and wakefulness (*79*). The relatively low number of c-Fos–positive cells in these regions suggests reduced spontaneous activity in the absence of external stimuli. Further experiments under LD or stimulus-driven conditions will be necessary to clarify these results.

Sensory systems also showed distinct circadian peak times. Although visual-related regions such as the SCs, LGd, and VISp4 peaked during the subjective day, auditory-related regions such as the IC and the AUDp peaked during the midsubjective night. The medial geniculate nucleus, ventral part (MGv), the primary auditory thalamic nucleus (*80*), also showed voxelwise peak times around CT17 to CT22, although no significant rhythmicity was detected at the regional level (figs. S8D and S10C). This peak time opposition may reflect functional adaptation to the environmental light-dark cycle, optimizing visual processing during daytime and auditory processing during nighttime, even under DD conditions.

Brain regions involved in feeding, such as the DMH, ARH, and NTS, peaked around the midsubjective night, consistent with the timing of food intake in nocturnal animals. The SO, which regulates water balance, peaked around the transition from the subjective day to night (fig. S9D). This rhythm may reflect SCN-mediated modulation of excitatory input to SO neurons, which increases vasopressin release and osmosensitivity during the late inactive phase (*81*).

Brainwide neural activity patterns reflect brain CT

The brain is an integrated system in which diverse regions are expected to operate in a spatiotemporally coordinated manner. Although previous studies have typically assessed the circadian dynamics of individual regions, how these dynamics relate to those of the rest of the brain has not been evaluated. We therefore calculated the cell count ratio for each region by dividing the number of c-Fos–positive cells in that region by the total number in the entire brain at each time point. Analysis of these ratios revealed that peak times were distributed throughout the circadian cycle. The brain CT of a sample could be inferred from the global distribution of cell count ratios across brain regions by adapting computational approaches originally developed for transcriptomic and metabolomic datasets (*48*–*50*). This suggests that brainwide activity patterns not only reflect local circadian rhythms but also provide a readout of the organism's internal CT.

Although our dataset was obtained under controlled conditions in mice, this approach offers the possibility of using global activity patterns as a readout of brain state in broader contexts. A similar strategy was recently used to infer internal CT from spatially resolved transcriptomic data in human postmortem brains (*82*). This may inform future efforts to evaluate circadian disruption or temporal misalignment in disease models, pharmacological studies, or behavioral paradigms where time-resolved sampling is not feasible.

The database provides a temporal reference of brainwide neural activity for neuroscience and other research

The dataset from this study is freely available online to support further research. It is compatible with a wide range of existing resources, including those for gene expression, anatomical connectivity, and cell-type distributions (*26*, *73*, *83*, *84*). This compatibility enables future integrative analyses that combine spatially resolved circadian neural activity with transcriptomic, connectomic, and epigenomic data.

Understanding the magnitude of circadian neural activity in brain regions is essential for designing and interpreting neuroscience experiments, as well as therapeutic studies. The efficacy of pharmacological treatments for cancer and other common diseases can vary significantly depending on the time of day (*85*, *86*). Similarly, the therapeutic effects of psychiatric medications such as antidepressants may depend on the timing of administration (*87*). Our study highlights the possibility that brain-targeted therapies could exhibit time-of-day–dependent effects based on the circadian rhythm of the target regions. A brainwide understanding of circadian neural activity may therefore contribute to identifying optimal timing for therapeutic interventions and enhancing treatment efficacy.

Limitations of c-Fos as a marker for neural activity

The *c-fos* gene is an IEG that is transcribed rapidly in response to stimulation without requiring de novo protein synthesis. In the central nervous system, c-Fos is induced by diverse stimuli, and its transcription is driven by the Ca^{2+}/cAMP response element in its promoter, which is activated by intracellular Ca^{2+} influx through Ca^{2+}-dependent kinases

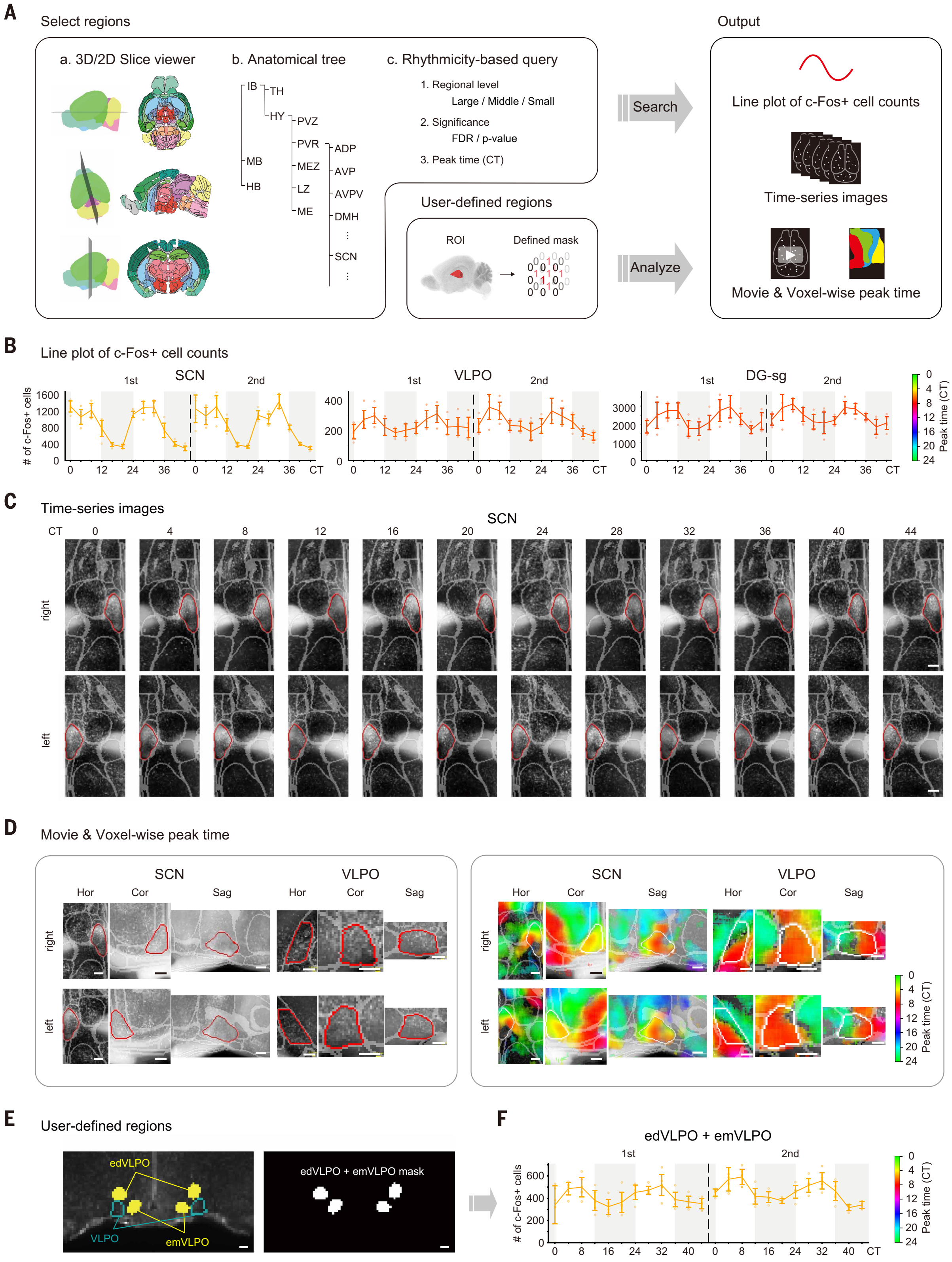

Fig. 6. Open-access database of whole-brain circadian c-Fos data. (**A**) Schematic overview of region selection and output options. Users can select regions by typing region names in a text box or using one of three options: (a) a 3D/2D slice viewer, (b) an anatomical tree, or (c) a rhythmicity-based query using regional level, statistical significance, and peak time. Users can also define regions by drawing ROIs and converting them into binary masks using common image analysis software for rhythmicity analysis. Output options include line plots of c-Fos–positive cell counts, time-series images, and both time-series movies and voxelwise peak time visualizations. For user-defined regions, only line plots are currently supported. (**B**) Database output: line plots of c-Fos–positive cell counts in selected regions. Colors represent peak time. SCN (abbreviated as SCH in the database following the Allen Brain Atlas), suprachiasmatic nucleus; DG-sg, dentate gyrus, supragranular layer; VLPO, ventrolateral preoptic nucleus. (**C**) Database output: horizontal projection of time-series c-Fos images of the SCN and its surrounding areas averaged from six samples in the first experiment. Red and translucent white outlines

denote the SCN and its surrounding regions, respectively. Scale bar, 200 μm. (**D**) Database output: time-series c-Fos movies and voxelwise peak time images of the SCN and VLPO, shown as horizontal, coronal, and sagittal projections. The regions are outlined in red (movies) or white (voxelwise images), with translucent white for surrounding regions. In the voxelwise peak time images, colors represent peak time and transparency reflects rhythmicity. Scale bar, 200 μm. (**E**) Example mask of user-defined regions. Left: manually defined regions adjacent to the extended dorsal and medial sides of the VLPO (green; edVLPO and emVLPO, respectively), shown with the original VLPO from the database (red border) in a coronal section. Right: corresponding binary mask of edVLPO and emVLPO. Scale bar, 200 μm. (**F**) Database output: line plot of c-Fos–positive cell counts in the edVLPO and emVLPO showing a peak around CT5.3. Color represents peak time.

and the transcription factor cAMP response element-binding protein (CREB). Because Ca^{2+} influx is a fundamental feature of neuronal activity, c-Fos has been widely used as an indirect marker of neural activation.

However, one limitation of c-Fos as an activity marker is the temporal delay between neural activity and detectable expression. Given the dynamics of c-Fos expression, with protein levels peaking within 1 to 2 hours after stimulation and a half-life of ~1.5 to 2 hours (*17*, *88*, *89*), the peak time of c-Fos protein likely reflects neural activity that peaked ~2 to 3 hours earlier or alternatively sustained activity over a broader time window. Thus, circadian c-Fos dynamics in our study should be interpreted as a temporally lagged and cumulative representation of neural activity. Moreover, c-Fos is not suitable for capturing faster dynamics such as those underlying REM sleep or intrahippocampal signaling relevant to memory processes. Accordingly, the grouping based on physiological functions in our analysis should be viewed as highlighting circadian trends rather than as direct evidence of circadian modulation of those rapid processes. Another limitation arises from the small number of c-Fos–positive cells in regions, which may hinder the detection of significant rhythmicity. For instance, in the LC, c-Fos–positive cell counts remained low across the circadian cycle, although voxelwise analysis showed subregional rhythmicity. Furthermore, c-Fos induction depends not only on neural activity but also on intracellular signaling pathways and neuromodulatory factors (*90*). In addition, c-Fos is not strictly neuron specific and can also be expressed in nonneuronal cells. A further limitation is that c-Fos expression can be strongly influenced by sleep-wake states. Because circadian regulation and sleep-wake states are tightly and bidirectionally coupled (*59*), these influences are inherently difficult to disentangle. Accordingly, the "peak times" reported here should be interpreted as reflecting both circadian drive and sleep-wake states under constant darkness.

Despite these limitations, our study demonstrates that whole-brain, time-series c-Fos mapping provides a spatially comprehensive view of circadian rhythmicity in neural activity. This brainwide circadian atlas not only enhances our understanding of temporal neural coordination but also provides a new foundation for integrating time-of-day information into neuroscience and pharmacological research.

Materials and methods

Mice

Male C57BL/6N mice (CLEA, Japan) were used for sampling at 10 weeks of age. Two experiments were performed, using a total of 144 mice. All experimental procedures and housing conditions were approved by the Animal Care and Use Committee of RIKEN. All animals were handled humanely in accordance with institutional guidelines.

Time-series brain sampling

After one week of acclimation in standard group housing conditions under a 12-hour light/dark (LD) cycle at constant temperature and humidity, the mice were individually housed in cages equipped with Snappy Sleep Stager (SSS) (*91*), a noninvasive sleep/wake recording system based on respiratory measurements. They were maintained under the LD cycle for 2 weeks before the experiment, after which the lighting condition was changed to DD. Sampling was performed every 4 hours from CT0 to CT44, covering 12 time points over a 48-hour period. At each time point, the SSS rack door was opened 10 min prior, and six mice were simultaneously anesthetized in their cages using isoflurane delivered through an air system for 2 min to induce deep anesthesia. To minimize stimulation-induced c-Fos expression, the mice were immediately subjected to perfusion and fixation, as c-Fos becomes detectable ~20 min after stimulation (*88*). The mice were perfused with phosphate-buffered saline (PBS) containing heparin (10 U/ml), followed by fixation with 4% paraformaldehyde (PFA) in PBS. The entire process, from opening the SSS rack door to completing the perfusion and fixation of all six mice, was completed within 20 min. Thus, although isoflurane can influence c-Fos expression, its impact in this experiment is expected to be minimal, although it cannot be fully excluded. The brains were then extracted and post-fixed in 4% PFA in PBS for 20 hours at 4°C.

Tissue clearing and immunostaining

Tissue clearing and immunostaining were performed according to the CUBIC-HistoVIsion 1.0 protocol described by Susaki *et al.* (*23*), with some modifications. Fixed brains were first delipidated in CUBIC-L solution for five days (50% for one day, 100% for four days). After three washes with PBS, 72 samples were simultaneously stained in 3D with the nuclear dye SYTOX Green for atlas mapping during image analysis. After three washes with 10 mM HEPES and replacement with staining buffer, the samples were stained with a complex of anti-rabbit anti-c-Fos antibody (0.5 μg/sample, Abcam, ab222699) and Alexa Fluor 594-labeled secondary Fab fragment (3:4 weight ratio) at 37 °C for three weeks, with the final day at 4 °C. After brief washes with 0.1 M phosphate buffer (PB) containing 10% Triton X-100 followed by PB alone, the samples were post-fixed in 1% formalin in PB for 24 hours. After a PB wash, the samples were cleared in CUBIC-R+ solution for five days (50% for one day, 100% for four days). For imaging, each brain was embedded in CUBIC-R+ gel in a 6-well plate (*92*).

Imaging

The whole-brain samples were imaged using a custom-built light-sheet microscope constructed in our laboratory (*92*). A 0.63× objective lens was used, with each pixel in the xy-plane corresponding to 10 μm × 10 μm, and z-stacks were acquired with a 10 μm step size. A 488 nm laser was used for SYTOX Green (laser power: 200 mW, exposure time: 20 ms), and a 592 nm laser was used for c-Fos (laser power: 300 mW, exposure time: 200 ms). A 625/25 nm emission filter was used for both channels.

Image data preprocessing

Raw c-Fos staining images were normalized by calculating the median voxel intensity within the brain volume for each sample, using only voxels with intensities above 5,000 to exclude voxels outside the brain. Each voxel value was then scaled so that the median intensity became 10,000, within a 16-bit dynamic range (0–65,535). To generate high-resolution images for cell detection, the normalized c-Fos immunostaining images were upsampled 2.5-fold and deconvolved using the Richardson–Lucy algorithm (*93*).

Peak detection

As the first step in detecting c-Fos–positive cells, every voxel with intensity greater than 5,000 was evaluated and defined as a peak if it showed the highest intensity within the surrounding 7 × 7 × 7 voxel neighborhood in the deconvolved images. As described in our previous work (*92*), a 3 × 3 × 3 voxel kernel was used for peak detection, corresponding to the approximate size of a single cell at the original resolution. In this study, a 7 × 7 × 7 voxel kernel was applied after 2.5-fold upsampling (from 10 μm to 4 μm voxels) to maintain a comparable physical scale. This kernel size ensures consistency with prior protocols while balancing resolution and noise robustness.

Peak filtering and feature calculation

To characterize each candidate peak, the corresponding background minimum intensity was defined as the lowest voxel value within an 11 × 11 × 11 voxel neighborhood centered on each peak, to quantify the local contrast between the peak and its surrounding background. This kernel size corresponds to a 2.5-fold upsampling of the 5 × 5 × 5 voxel window used in our previous work (92). The intensity ratio (*ratioI*) was defined as the ratio of the center voxel intensity to the minimum intensity (i.e., center voxel intensity divided by minimum intensity). To construct the distribution of $\log_{10}(ratioI)$ values used for thresholding, ~10% of all peaks detected across 144 samples (3,571,055,045 peaks in total) were randomly selected. The distribution of $\log_{10}(ratioI)$ of the peaks was plotted and fitted with a Gaussian mixture model (fig. S2A). Assuming that the Gaussian component with the lower mean represented noise peaks and the one with the higher mean represented c-Fos–positive peaks, a threshold of *ratioI* corresponding to a false positive rate of 0.5% (~1.385) was determined. Peaks exceeding this threshold were defined as filtered peaks and considered candidates for c-Fos–positive cells.

To distinguish true c-Fos–positive cells from other structures, machine learning-based cell classification was applied. Fifteen features were computed for each filtered peak. Ten of these features were derived from distance functions comparing the 11 × 11 × 11 voxel local volume centered on each peak (normalized by its maximum and minimum intensities) to a set of 81 idealized point spread function (PSF)-based template images. These templates were generated as follows: a synthetic point was placed at the center of a 23 × 23 × 23 voxel space and then shifted by one voxel in each of the x, y, and z directions, resulting in 27 variations. Gaussian filters with three different sets of sigma values were applied to these points to simulate varying PSF contrasts, and the resulting images were downsampled by a factor of 2 in each dimension to yield 11 × 11 × 11 voxel templates.

The 10 distance functions were defined as follows (94, 95):

$$\text{Hellinger coefficient } \sum_x P(x)Q(x)$$

$$\text{Chernoff coefficient } \sum_x P(x)^{P(x)}Q(x)^{(1-P(x))}$$

$$\text{Jeffreys distance } \sum_x \left(\sqrt{P(x)}-\sqrt{Q(x)}\right)^2$$

$$\text{Directed divergence } \sum_x P(x)log2\left(\frac{P(x)}{Q(x)}\right)$$

$$\text{Jensen (J) divergence } \sum_x (P(x)-Q(x))log2\left(\frac{P(x)}{Q(x)}\right)$$

$$\text{L1 norm } \sum_x |P(x)-Q(x)|$$

$$\text{L2 norm } \sum_x \sqrt{(P(X)-Q(X))^2}$$

$$\text{Kullback-Leibler (KL) divergence } \sum_x P(x)log10\left(\frac{P(x)}{Q(x)}\right)$$

$$\text{Pearson's chi-squared statistic } \sum_x \frac{(P(x)-Q(x))^2}{P(x)} \quad (P(x)!=0) \ \ else \ \ 0$$

$$\text{Jensen-Shannon (JS) divergence}$$

$$\sum_x P(x)log10\left(\frac{P(x)}{M}\right)+Q(x)log10\left(\frac{Q(x)}{M}\right),\ M=\frac{(P(x)+Q(x))}{2}$$

where P and Q are functions representing probability distributions. x is a value within the domain of the probability distributions. For each distance function, the minimum value across the 81 comparisons was used as the final feature value. In addition to these 10 distance-based features, *ratioI* and *deltaI* (defined as center voxel intensity minus minimum intensity) were included for each candidate.

Furthermore, to account for the spatial symmetry of the local volumes, the tensor of inertia was calculated for each normalized volume using the following equations:

$$I = \left(I_{xx}\, I_{xy}\, I_{xz}\, I_{yx}\, I_{yy}\, I_{yz}\, I_{zx}\, I_{zy}\, I_{zz}\right)$$

$$I_{xx} = \sum_i m_i\left(y_i^2+z_i^2\right) I_{yy} = \sum_i m_i\left(x_i^2+z_i^2\right)$$

$$I_{zz} = \sum_i m_i\left(x_i^2+y_i^2\right) I_{xx} = \sum_i m_i\left(y_i^2+z_i^2\right) I_{xy} = I_{yx} = -\sum_i m_i x_i y_i$$

$$I_{xz} = I_{zx} = -\sum_i m_i x_i z_i I_{yz} = I_{zy} = -\sum_i m_i y_i z_i$$

m_i is the set of normalized voxel intensities in the candidate local volume, and (x_i, y_i, z_i) are the coordinates of each voxel relative to the center. The inertia tensor encodes the 3D shape and orientation of the intensity distribution within the ROI. Because its diagonal elements are the simplest summary of how wide or elongated the volume is along each axis, diagonal components of this tensor (I_{xx}, I_{yy}, I_{zz}) were also included as features.

Collecting training and test datasets

To enable consistent cell detection across all brain samples and regions, training and test datasets for supervised learning were constructed using one sample at CT0, CT8, and CT16 from both the first and second experiments. In each sample, at least 200 candidate peaks were manually labeled as either "c-Fos positive" or "c-Fos negative" (e.g., unlabeled cells, fibers, vessels, or background structures) in each of four regions—the SCN, CP (caudoputamen), CA1, and SSp-m2/3 (primary somatosensory area, mouth, layer 2/3) (fig. S2B). Distributions of the 15 features for "c-Fos positive" and "c-Fos negative" peaks are shown in fig. S3A. Additionally, to reduce false positives along the brain surface, some of these candidates were labeled as "c-Fos negative" and added to the training dataset. Furthermore, because saturated signals appear flattened due to uniformly high intensities and may be misclassified as negative, the candidates nearest to the centroid were labeled as "c-Fos positive" and added to the training dataset. Final training dataset compositions are shown in table S1.

Training and evaluating models

The annotated dataset was randomly split into training and test sets at a 7:3 ratio. The following machine learning models were trained on the training set and evaluated on the test set: Logistic Regression, Support Vector Machine (SVM), k-Nearest Neighbors (KNN), Random Forest, Decision Tree, Multi-Layer Perceptron (MLP), Naive Bayes, eXtreme Gradient Boosting (XGBoost), and Adaptive Boosting (AdaBoost).

F1 scores were compared across models and the one with the highest score was selected (fig. S4A). XGBoost outperformed the others and was further optimized using Bayesian hyperparameter tuning within the parameter ranges listed in tables S2 and S3. To avoid overfitting, 5-fold cross-validation was applied. The feature importance from the final model and F1 scores by region in the test set and are shown in figs. S3B and S4B.

Using the trained XGBoost model, all candidates in the 144 samples were classified as either "c-Fos positive" or "c-Fos negative," and the classification results were visually validated.

Registration and transformation of images and cell coordinates

To enable region-based analysis, the positions of c-Fos–positive cells were registered to a common anatomical framework. The normalized c-Fos and nuclear staining images of each sample were downsampled to one-fifth of the original resolution, resulting in an effective voxel size of 50 μm. For consistency across samples, the median intensity of each nuclear staining image was scaled to a common value before registration. The downsampled nuclear images were registered to the CUBIC-R+-treated reference atlas (Neuron Atlas) using Advanced Normalization Tools (ANTs) (*96*), with parameters based on our previous study (*97*). The same transformation was applied to the downsampled c-Fos images and the coordinates of detected c-Fos–positive cells. All c-Fos–positive cells were then annotated with anatomical region IDs from the Allen Brain Atlas (CCFv3) (*26*).

Generating higher-resolution ANTs-transformed images

To enable voxelwise analysis, all voxel values from the normalized c-Fos staining image of each sample were transformed into the Neuron Atlas space using the transformation matrix obtained from the previous registration. For generating higher-resolution ANTs-transformed images in Figs. 4, B and C, and 6, C and D, and figs. S10, B and C, and S14, these transformed values were subsequently downsampled by a factor of 2, resulting in a voxel size of 20 μm.

Circadian rhythmicity analysis using analytic cosinor test

Circadian rhythmicity was evaluated assuming a 24-hour oscillation period, which provides a reasonable approximation of circadian rhythms under our experimental conditions. Two 48-hour time series were concatenated into one virtual 96-hour time series to identify reliable oscillatory patterns that recurred with consistent phase. Because the time series spans 96 hours, periodicities of 48, 32, 24, 19.2, 16 hours, etc., can theoretically be detected, corresponding to two, three, four, five, and six full cycles. Among these, the 24-hour component was specifically tested, enabling a straightforward interpretation of oscillation phases.

To analyze the rhythmicity of c-Fos–positive cell counts in each region or voxel, a computationally efficient cosinor analysis was developed, referred to as the analytic cosinor test. This method analytically derives P values under a null distribution, thereby avoiding computationally heavy permutations, and provides both statistical significance and oscillation phase at a specified period. It is built on the same geometric principles as Fisher's G-test (*98*), but whereas Fisher's G-test scans across multiple frequencies, the analytic cosinor test efficiently evaluates a single predefined period (e.g., 24 hours). This targeted design yields three key advantages: (i) simplified mathematical formulation, (ii) markedly faster computation, and (iii) intuitive incorporation of measurement errors. The derivation is outlined below.

A linear combination of sine and cosine functions of a given period can be used to generate a sinusoid with arbitrary phase. The weights of this combination are obtained by projecting the waveform onto the sine and cosine functions. The ratio of these weights defines the oscillation phase, and their norm reflects similarity to a sinusoid. These properties underlie Fourier transformation. The norm is equivalent to Pearson's correlation when the waveform, sine, and cosine vectors are zero-mean and unit-normalized. Accordingly, Pearson's correlation (L) of the time series data with the sinusoidal waveform was defined as:

$$L = \sqrt{\left(\overrightarrow{X}\cdot\overrightarrow{B_s}\right)^2 + \left(\overrightarrow{X}\cdot\overrightarrow{B_c}\right)^2},$$

where $\overrightarrow{X}$, $\overrightarrow{B_s}$, and $\overrightarrow{B_c}$ are vectors representing the time-series data, sine curve, and cosine curve, respectively. Each vector was normalized to have a unit length. The oscillation phase (φ) of $\overrightarrow{X}$ is given by:

$$\varphi = \arctan\left(\overrightarrow{X}\cdot\overrightarrow{B_s}, \overrightarrow{X}\cdot\overrightarrow{B_c}\right).$$

To evaluate the statistical significance of a given correlation (L), the null distribution of random waveforms was considered. With n data points, a random vector consists of n independent and identically distributed (i.i.d.) Gaussian variables. After normalization, these vectors are uniformly distributed on the surface of a unit sphere in $(n - 1)$-dimensional space, because one degree of freedom is removed by the unit-length constraint.

Notice that the sine and cosine curves, $\overrightarrow{B_s}$ and $\overrightarrow{B_c}$, are also vectors on this $(n - 1)$-dimensional unit sphere. These two vectors span a plane in the $(n - 1)$-dimensional space, and the length of the projected vector of the waveform onto this plane represents the Pearson's correlation with the closest sinusoid among all oscillation phases, whereas the direction of the projected vector represents the oscillation phase. Thus, waveform vectors with a correlation L are those that project onto the circumference of a circle with radius L on the plane. Equivalently, such vectors are distributed on the intersection of the $(n - 1)$-dimensional sphere and a cylinder extending perpendicularly from this circle. This intersection can be described, without loss of generality, as:

$$x_1^2 + x_2^2 + x_3^2 + \ \dots\ + x_{n-1}^2 = 1$$

$$x_1^2 + x_2^2 = L^2$$

$$\Rightarrow$$

$$x_3^2 + \ \dots\ + x_{n-1}^2 = 1 - L^2.$$

This shows that the intersection in $(n - 1)$-dimensional space is equivalent to the surface of a sphere with radius $\sqrt{1 - L^2}$ in $(n - 3)$-dimensional space. Vectors with correlation r greater than L are distributed inside this $(n - 3)$-dimensional sphere, because their coordinates satisfy:

$$x_3^2 + \ \dots\ + x_{n-1}^2 < 1 - r^2 \quad (r > L).$$

Therefore, the probability of obtaining Pearson's correlation greater than L from random waveforms is given by the ratio of the volume of this sphere to that of the unit sphere, hence:

$$P(r > L) = \frac{V_{n-3}\left(\sqrt{1-L^2}\right)}{V_{n-3}(1)}.$$

Because the volume of an m-dimensional sphere is given by:

$$V_m(r) = \frac{\pi^{m/2}}{\Gamma(m/2+1)}r^m,$$

the probability simplifies to:

$$P(L) = \left(1-L^2\right)^{\frac{n-3}{2}}.$$

This gives the probability of obtaining a Pearson's correlation greater than or equal to L from random waveforms.

A reference Python implementation of the analytic cosinor test is archived at Zenodo (*99*).

Although the present analysis focused on the 24-hour period, the cosinor test retains broad sensitivity around this period. Pure sinusoids with periods between 21 and 27 hours yielded P values below 0.01 (fig. S16), indicating practical coverage of circadian-range oscillations.

To account for measurement errors at each time point, the projected vector length was reduced according to the error magnitude. Errors were modeled as an ellipsoid with radii of 0.0375 × SEM along each axis at the tip of the waveform vector in the $(n - 1)$-dimensional space. The factor 0.0375 corresponds to the radius of a 3% confidence interval. The ratio of the waveform vector reaching the ellipsoid was used to scale down the projected vector length, thereby conservatively adjusting the P value. To assess robustness, we also varied the confidence interval radius factor to 10% (0.126 × SEM), 30% (0.385 × SEM), and 50% (0.674 × SEM). The number of regions classified as rhythmic (FDR < 0.1) changed slightly, from 508 at 3% to 503, 492, and 479, respectively (table S4), indicating that the main conclusions remain robust to the confidence interval setting.

We also evaluated alternative analysis schemes without concatenating the two time-series datasets. These included (i) four independent 1-day analyses with P values combined (FDR < 0.1: 26 regions), (ii) a single 24-sample analysis across 6 time points (0 regions), (iii) two 12-time-point analyses with *P* values combined (409 regions), and (iv) a single 12-sample analysis across 12 time points (312 regions). In all cases, fewer regions showed significant rhythmicity, reflecting reduced statistical power of shorter or split time courses. Concatenating the two DD time courses allowed sensitive detection of circadian oscillations with consistent phase. In this analysis, a 24-hour period was used to approximate the circadian rhythm observed in mice under DD conditions.

Statistical results from the analytic cosinor test across 642 brain regions are summarized in table S4, including the Benjamini–Hochberg adjusted *q* value (BH.Q; corresponding to the FDR used in the manuscript), adjusted *P* value (ADJ.P), peak phase (Ph, in radians), time lag (LAG), and maximum correlation coefficient (max_corr), along with c-Fos–positive cell counts for each of the 144 samples.

The results obtained using this method were compared with those from the JTK_CYCLE, a widely used approach for evaluating rhythmic gene expression (*25*). The number of significantly rhythmic regions (508 at FDR < 0.1 for the analytic cosinor test and 549 at FDR < 0.05 for JTK_CYCLE) was not markedly different between the two methods (fig. S6A and table S6). These results, together with robustness checks at alternative confidence interval settings, support the use of a 3% confidence interval in the present analysis. When circadian peak phases estimated by both methods were compared, the analytic cosinor test appeared to perform comparably to JTK_CYCLE (fig. S6B). Because of this computational simplicity, the analytic cosinor test enables much faster analysis, providing a practical approach for voxelwise analysis.

Voxelwise rhythmicity analysis

To investigate circadian rhythms of c-Fos–positive cell counts in greater detail, voxelwise rhythmicity analysis was performed at a 20-μm voxel scale. For each voxel, the number of c-Fos–positive cells was calculated as the total within a 160-μm cubic volume centered on that voxel (fig. S10A). This convolution step was introduced to reduce the influence of registration misalignment during image normalization and to enhance the robustness of rhythmicity detection in subregions. Rhythmicity across all voxels in the whole brain was assessed using the analytic cosinor test, after concatenating the two consecutive circadian cycles into a 4-day series. Each voxel was color-coded according to its peak time, and transparency was scaled based on the FDR (Figs. 4B and 6C and fig. S10C). To visualize peak time distributions, voxelwise color maps were overlaid on representative averaged c-Fos images at CT0 ($n = 6$, first experiment). Results obtained with different convolution sizes are presented in fig. S10B.

Predicting brain CT using the timetable method

The timetable method was described previously (*48*). The cell count ratio for each brain region was calculated by dividing the c-Fos–positive cell count in that region by the total c-Fos–positive cell count in the entire brain at each time point (Fig. 5A). For each rhythmic brain region i ($i = 1\ldots N$), c-Fos–positive cell count ratio X_i was normalized using its mean (μ_i) and standard deviation (σ_i; SD) derived from the regional timetable. The normalized value Y_i was defined as:

$$Y_i = \left(X_i - \mu_i\right) / \sigma_i$$

A profile $\left\{t_i, Y_i\right\}$ was then constructed, where t_i denotes the peak time of region i. To predict brain CT, the correlation between this profile and a 24-hour cosine function $\left\{t_i, \sqrt{2}\cos\left(2\pi\left(t_i - b\right)/24\right)\right\}$ was calculated across all regions, where b ($0 \leq b < 24$) represents the phase. The amplitude was fixed at 2 so that the SD of the cosine waveform matched that of Y_i. The phase b that yielded the highest correlation coefficient c was selected, and the corresponding phase b_c was taken as the predicted brain CT.

In Fig. 5, C and D, this method was applied to 216 significantly rhythmic regions with homogeneously distributed relative peak times across the 24-hour cycle (fig. S12B). To ensure phase balance, 25 regions with the lowest FDR were selected from each of the 24 phase bins. If fewer than 25 regions were available in a bin, all were included. Brain CT for each sample was predicted using the remaining samples.

Sensitivity and specificity of the timetable method

The sensitivity and specificity of the timetable method were evaluated using regions selected at different FDR thresholds (fig. S12, H and I). To determine a correlation cutoff value for each threshold, 10 samples were randomly selected, and control profiles of cell count ratios incorporating 100% measurement noise were generated for each sample. The average correlation cutoff value (cth_{ave}) was then computed from these 10 samples.

For each sample, a random cell count ratio profile $\left\{t_i, Y_r\right\}$ ($i = 1\ldots N$) was generated, where Y_r is a random variable following the distribution of Y_i. The correlation value (c^r) and phase (b_r) of the best-fitted cosine curve were subsequently calculated as described above. This procedure was repeated 10,000 times to establish the distribution of correlation values c^r and phases b_c^r.

Similarly, a control cell count ratio profile with 100% measurement noise $\left\{t_i, \sqrt{2}\cos\left(2\pi\left(t_i/24\right)\right) + d_r\right\}$ ($i = 1\ldots$ N) was generated, where d_r is a random variable following the distribution of d_i. The correlation value (c^c) and phase (b_c) of the best-fitted cosine curve were calculated for each control profile, and this process was also repeated 10,000 times to generate the distribution of correlation values c^c and the phases b_c^c.

Measurement noise was defined as the SD of d_i across all selected rhythmic regions at a given FDR threshold, where $d_i = Y_i - \sqrt{2}\cos\left(2\pi\left(t_i - b_c\right)/24\right)$ and b_c represents the predicted brain CT. From the distributions of c^c and c^r, probability values P_c or P_r were determined at each correlation threshold c. Sensitivity S_c was defined as

$$S_c(c) = 1 - P_c(c),$$

and specificity S_r was defined as

$$S_r(c) = 1 - P_r(c).$$

These metrics were used to construct receiver operating characteristic (ROC) curves for the timetable method using rhythmic regions under 100% measurement noise. A correlation cutoff value c ($0 \leq c \leq 1$) was identified for each of the 10 selected samples where sensitivity and specificity were equal $\left[S_r(c) = S_c(c)\right]$. The average correlation cutoff value (cth_{ave}) was then calculated across these samples.

To assess sensitivity, the best correlation value was calculated for each of the 144 samples using the remaining samples, as described above. Sensitivity was defined as the percentage of cell count ratio profiles ($n = 144$) with correlation values exceeding the average cutoff value cth_{ave}. For specificity, random cell count ratio profiles $\left\{t_i, Y_r\right\}$ ($i = 1\ldots N$) were generated for each of the 144 samples, where Y_r is a random variable following the distribution of Y_i. The best correlation value was calculated for each random profile using the same method. Specificity was defined as the percentage of these random profiles with correlation values below cth_{ave}.

Predicting brain CT using CYCLOPS 2.0

CYCLOPS 2.0, a cyclic ordering algorithm described previously (*50*), was used to predict brain CT of samples. This method rearranges samples along an elliptical trajectory based on high-dimensional input data. Cell count ratios of all brain regions across the 144 samples were provided as input.

Prediction accuracy was evaluated under different parameter settings. These included the minimum and maximum coefficients of variation (CV) for selecting seed regions (seed_min_CV and seed_max_CV), the minimum number of seed regions to include based on descending average cell count ratio (seed_mth_Region), and the maximum number of dimensions used in the eigen decomposition (eigen_max). For each parameter set, the error between true sampling times and predicted brain CT was calculated (fig. S12, J to N).

Architecture of the whole-brain circadian activity database

An open-access database was constructed and hosted on a website. The backend was implemented using the Python Flask framework, and the frontend was developed with HTML and JavaScript. Three-dimensional objects and planes in the slice viewer were generated using Three.js. Two-dimensional images were produced by slicing the Neuron Atlas at 5-μm steps. Anatomical divisions in the database correspond to the hierarchical anatomical ontology of the Allen Brain Mouse Atlas (*26*).

User-defined ROI analysis of circadian c-Fos expression

User-defined ROIs were created as binary masks (TIFF format; shape: 243 × 440 × 339 [z, y, x], 8-bit), with 1 indicating the region and 0 elsewhere. The Neuron Atlas nuclear staining images and the corresponding atlas region ID images are available on Zenodo (*100*) as reference resources for user-defined ROI definition. As a demonstration, extended regions adjacent to the dorsal and medial borders of the VLPO, called edVLPO and emVLPO, respectively, were manually defined based on anatomical references (*51*). ROIs were drawn and filled using ImageJ. For each of the 144 samples, c-Fos–positive cells within the masked areas were counted, and circadian rhythmicity was evaluated using the analytic cosinor test.

Software

All analysis, except for voxelwise counting of c-Fos–positive cells, were performed using Python 3.8 and its associated libraries (Numpy, Numba, SciPy, Pandas, Matplotlib, Seaborn, NiBabel, Tifffile, scikit-image, scikit-learn, and XGBoost). Voxelwise cell counting was performed using C++17 and CUDA (version 12.0) on a GPGPU environment (NVIDIA RTX A5000 or A6000).

Color-blind–accessible figures

To improve accessibility for color-blind readers, we prepared supplementary versions of the main figures (Figs. 1 to 6) and supplementary figures (figs. S6 to S11 and S14), provided as figs. S17 to S29, using a color map optimized for individuals with color vision deficiencies.

REFERENCES AND NOTES

1. J. S. Takahashi, H.-K. Hong, C. H. Ko, E. L. McDearmon, The genetics of mammalian circadian order and disorder: Implications for physiology and disease. *Nat. Rev. Genet.* **9**, 764–775 (2008). doi: 10.1038/nrg2430; pmid: 18802415
2. J. A. Evans, A. J. Davidson, Health consequences of circadian disruption in humans and animal models. *Prog. Mol. Biol. Transl. Sci.* **119**, 283–323 (2013). doi: 10.1016/B978-0-12-396971-2.00010-5; pmid: 23899601
3. E. E. Abrahamson, R. Y. Moore, Suprachiasmatic nucleus in the mouse: Retinal innervation, intrinsic organization and efferent projections. *Brain Res.* **916**, 172–191 (2001). doi: 10.1016/S0006-8993(01)02890-6; pmid: 11597605
4. D. K. Welsh, J. S. Takahashi, S. A. Kay, Suprachiasmatic nucleus: Cell autonomy and network properties. *Annu. Rev. Physiol.* **72**, 551–577 (2010). doi: 10.1146/annurev-physiol-021909-135919; pmid: 20148688
5. S. Yamaguchi *et al.*, Synchronization of cellular clocks in the suprachiasmatic nucleus. *Science* **302**, 1408–1412 (2003). doi: 10.1126/science.1089287; pmid: 14631044
6. E. D. Herzog, T. Hermanstyne, N. J. Smyllie, M. H. Hastings, Regulating the suprachiasmatic nucleus (SCN) circadian clockwork: Interplay between cell-autonomous and circuit-level mechanisms. *Cold Spring Harb. Perspect. Biol.* **9**, a027706 (2017). doi: 10.1101/cshperspect.a027706; pmid: 28049647
7. S. Wen *et al.*, Spatiotemporal single-cell analysis of gene expression in the mouse suprachiasmatic nucleus. *Nat. Neurosci.* **23**, 456–467 (2020). doi: 10.1038/s41593-020-0586-x; pmid: 32066983
8. L. Xie *et al.*, Cholecystokinin neurons in mouse suprachiasmatic nucleus regulate the robustness of circadian clock. *Neuron* **111**, 2201–2217.e4 (2023). doi: 10.1016/j.neuron.2023.04.016; pmid: 37172583
9. K. Begemann, A.-M. Neumann, H. Oster, Regulation and function of extra-SCN circadian oscillators in the brain. *Acta Physiol. (Oxf.)* **229**, e13446 (2020). doi: 10.1111/apha.13446; pmid: 31965726
10. L. Renouard *et al.*, The supramammillary nucleus and the claustrum activate the cortex during REM sleep. *Sci. Adv.* **1**, e1400177 (2015). doi: 10.1126/sciadv.1400177; pmid: 26601158
11. J. C. Gonzalez *et al.*, Circadian regulation of dentate gyrus excitability mediated by G-protein signaling. *Cell Rep.* **42**, 112039 (2023). doi: 10.1016/j.celrep.2023.112039; pmid: 36749664
12. G. F. Turi *et al.*, Serotonin modulates infraslow oscillation in the dentate gyrus during non-REM sleep. *eLife* **13**, RP100196 (2025). doi: 10.7554/eLife.100196; pmid: 40178074
13. N. Renier *et al.*, iDISCO: A simple, rapid method to immunolabel large tissue samples for volume imaging. *Cell* **159**, 896–910 (2014). doi: 10.1016/j.cell.2014.10.010; pmid: 25417164
14. E. A. Susaki *et al.*, Whole-brain imaging with single-cell resolution using chemical cocktails and computational analysis. *Cell* **157**, 726–739 (2014). doi: 10.1016/j.cell.2014.03.042; pmid: 24746791
15. H. R. Ueda *et al.*, Tissue clearing and its applications in neuroscience. *Nat. Rev. Neurosci.* **21**, 61–79 (2020). doi: 10.1038/s41583-019-0250-1; pmid: 31896771
16. S. M. Sagar, F. R. Sharp, T. Curran, Expression of c-fos protein in brain: Metabolic mapping at the cellular level. *Science* **240**, 1328–1331 (1988). doi: 10.1126/science.3131879; pmid: 3131879
17. K. J. Kovács, Measurement of immediate-early gene activation- c-fos and beyond. *J. Neuroendocrinol.* **20**, 665–672 (2008). doi: 10.1111/j.1365-2826.2008.01734.x; pmid: 18601687
18. F. Weber, Y. Dan, Circuit-based interrogation of sleep control. *Nature* **538**, 51–59 (2016). doi: 10.1038/nature19773; pmid: 27708309
19. A. Franceschini *et al.*, Brain-wide neuron quantification toolkit reveals strong sexual dimorphism in the evolution of fear memory. *Cell Rep.* **42**, 112908 (2023). doi: 10.1016/j.celrep.2023.112908; pmid: 37516963
20. A. Sumová, Z. Trávnícková, J. D. Mikkelsen, H. Illnerová, Spontaneous rhythm in c-Fos immunoreactivity in the dorsomedial part of the rat suprachiasmatic nucleus. *Brain Res.* **801**, 254–258 (1998). doi: 10.1016/S0006-8993(98)00619-2; pmid: 9729414
21. J. P. Miller, J. D. McAuley, K. C. H. Pang, Spontaneous fos expression in the suprachiasmatic nucleus of young and old mice. *Neurobiol. Aging* **26**, 1107–1115 (2005). doi: 10.1016/j.neurobiolaging.2004.08.008; pmid: 15748791
22. M. Girotti, M. S. Weinberg, R. L. Spencer, Diurnal expression of functional and clock-related genes throughout the rat HPA axis: System-wide shifts in response to a restricted feeding schedule. *Am. J. Physiol. Endocrinol. Metab.* **296**, E888–E897 (2009). doi: 10.1152/ajpendo.90946.2008; pmid: 19190255
23. E. A. Susaki *et al.*, Versatile whole-organ/body staining and imaging based on electrolyte-gel properties of biological tissues. *Nat. Commun.* **11**, 1982 (2020). doi: 10.1038/s41467-020-15906-5; pmid: 32341345
24. H. Ueda *et al.*, "Whole-brain single-neuron atlas reveals microglial security hole accelerating neuronal vulnerability" (Research Square, 2025); https://doi.org/10.21203/rs.3.rs-5827312/v1.
25. M. E. Hughes, J. B. Hogenesch, K. Kornacker, JTK_CYCLE: An efficient nonparametric algorithm for detecting rhythmic components in genome-scale data sets. *J. Biol. Rhythms* **25**, 372–380 (2010). doi: 10.1177/0748730410379711; pmid: 20876817
26. Q. Wang *et al.*, The Allen Mouse Brain Common Coordinate Framework: A 3D Reference Atlas. *Cell* **181**, 936–953.e20 (2020). doi: 10.1016/j.cell.2020.04.007; pmid: 32386544
27. R. E. Brown, R. Basheer, J. T. McKenna, R. E. Strecker, R. W. McCarley, Control of sleep and wakefulness. *Physiol. Rev.* **92**, 1087–1187 (2012). doi: 10.1152/physrev.00032.2011; pmid: 22811426
28. S. Ren *et al.*, The paraventricular thalamus is a critical thalamic area for wakefulness. *Science* **362**, 429–434 (2018). doi: 10.1126/science.aat2512; pmid: 30361367
29. B. A. Sulaman, S. Wang, J. Tyan, A. Eban-Rothschild, Neuro-orchestration of sleep and wakefulness. *Nat. Neurosci.* **26**, 196–212 (2023). doi: 10.1038/s41593-022-01236-w; pmid: 36581730
30. T. E. Scammell, E. Arrigoni, J. O. Lipton, Neural circuitry of wakefulness and sleep. *Neuron* **93**, 747–765 (2017). doi: 10.1016/j.neuron.2017.01.014; pmid: 28231463
31. M. M. Halassa *et al.*, Selective optical drive of thalamic reticular nucleus generates thalamic bursts and cortical spindles. *Nat. Neurosci.* **14**, 1118–1120 (2011). doi: 10.1038/nn.2880; pmid: 21785436
32. R. G. K. Munn, D. K. Bilkey, The firing rate of hippocampal CA1 place cells is modulated with a circadian period. *Hippocampus* **22**, 1325–1337 (2012). doi: 10.1002/hipo.20969; pmid: 21830249
33. C. D. Clelland *et al.*, A functional role for adult hippocampal neurogenesis in spatial pattern separation. *Science* **325**, 210–213 (2009). doi: 10.1126/science.1173215; pmid: 19590004
34. M. Fyhn, S. Molden, M. P. Witter, E. I. Moser, M.-B. Moser, Spatial representation in the entorhinal cortex. *Science* **305**, 1258–1264 (2004). doi: 10.1126/science.1099901; pmid: 15333832
35. F. Ambroggi, A. Ishikawa, H. L. Fields, S. M. Nicola, Basolateral amygdala neurons facilitate reward-seeking behavior by exciting nucleus accumbens neurons. *Neuron* **59**, 648–661 (2008). doi: 10.1016/j.neuron.2008.07.004; pmid: 18760700

36. J. E. M. Byrne, M. E. Hughes, S. L. Rossell, S. L. Johnson, G. Murray, Time of day differences in neural reward functioning in healthy young men. *J. Neurosci.* **37**, 8895–8900 (2017). doi: 10.1523/JNEUROSCI.0918-17.2017; pmid: 28842409
37. L. J. Trejo, C. M. Cicerone, Cells in the pretectal olivary nucleus are in the pathway for the direct light reflex of the pupil in the rat. *Brain Res.* **300**, 49–62 (1984). doi: 10.1016/0006-8993(84)91340-4; pmid: 6733467
38. D. K. Morest, D. L. Oliver, The neuronal architecture of the inferior colliculus in the cat: Defining the functional anatomy of the auditory midbrain. *J. Comp. Neurol.* **222**, 209–236 (1984). doi: 10.1002/cne.902220206; pmid: 6699208
39. G. E. Alexander, M. D. Crutcher, Functional architecture of basal ganglia circuits: Neural substrates of parallel processing. *Trends Neurosci.* **13**, 266–271 (1990). doi: 10.1016/0166-2236(90)90107-L; pmid: 1695401
40. M. W. Howe, D. A. Dombeck, Rapid signalling in distinct dopaminergic axons during locomotion and reward. *Nature* **535**, 505–510 (2016). doi: 10.1038/nature18942; pmid: 27398617
41. W. Waespe, B. Cohen, T. Raphan, Dynamic modification of the vestibulo-ocular reflex by the nodulus and uvula. *Science* **228**, 199–202 (1985). doi: 10.1126/science.3871968; pmid: 3871968
42. J. Voogd, N. M. Gerrits, T. J. Ruigrok, Organization of the vestibulocerebellum. *Ann. N. Y. Acad. Sci.* **781**, 553–579 (1996). doi: 10.1111/j.1749-6632.1996.tb15728.x; pmid: 8694444
43. S. G. Lisberger, F. A. Miles, Role of primate medial vestibular nucleus in long-term adaptive plasticity of vestibuloocular reflex. *J. Neurophysiol.* **43**, 1725–1745 (1980). doi: 10.1152/jn.1980.43.6.1725; pmid: 6967953
44. M. W. Schwartz, S. C. Woods, D. Porte Jr., R. J. Seeley, D. G. Baskin, Central nervous system control of food intake. *Nature* **404**, 661–671 (2000). doi: 10.1038/35007534; pmid: 10766253
45. C. W. Bourque, Central mechanisms of osmosensation and systemic osmoregulation. *Nat. Rev. Neurosci.* **9**, 519–531 (2008). doi: 10.1038/nrn2400; pmid: 18509340
46. C. B. Saper, J. Lu, T. C. Chou, J. Gooley, The hypothalamic integrator for circadian rhythms. *Trends Neurosci.* **28**, 152–157 (2005). doi: 10.1016/j.tins.2004.12.009; pmid: 15749169
47. L. Talamanca, F. Naef, How to tell time: Advances in decoding circadian phase from omics snapshots. *F1000Res.* **9**, 1150 (2020). doi: 10.12688/f1000research.26759.1; pmid: 33014340
48. H. R. Ueda *et al.*, Molecular-timetable methods for detection of body time and rhythm disorders from single-time-point genome-wide expression profiles. *Proc. Natl. Acad. Sci. U.S.A.* **101**, 11227–11232 (2004). doi: 10.1073/pnas.0401882101; pmid: 15273285
49. Y. Minami *et al.*, Measurement of internal body time by blood metabolomics. *Proc. Natl. Acad. Sci. U.S.A.* **106**, 9890–9895 (2009). doi: 10.1073/pnas.0900617106; pmid: 19487679
50. R. C. Anafi, L. J. Francey, J. B. Hogenesch, J. Kim, CYCLOPS reveals human transcriptional rhythms in health and disease. *Proc. Natl. Acad. Sci. U.S.A.* **114**, 5312–5317 (2017). doi: 10.1073/pnas.1619320114; pmid: 28439010
51. D. Kroeger *et al.*, Galanin neurons in the ventrolateral preoptic area promote sleep and heat loss in mice. *Nat. Commun.* **9**, 4129 (2018). doi: 10.1038/s41467-018-06590-7; pmid: 30297727
52. J. H. Meijer, J. Schaap, K. Watanabe, H. Albus, Multiunit activity recordings in the suprachiasmatic nuclei: In vivo versus in vitro models. *Brain Res.* **753**, 322–327 (1997). doi: 10.1016/S0006-8993(97)00150-9; pmid: 9125419
53. K. E. van Esseveldt, M. N. Lehman, G. J. Boer, The suprachiasmatic nucleus and the circadian time-keeping system revisited. *Brain Res. Brain Res. Rev.* **33**, 34–77 (2000). doi: 10.1016/S0165-0173(00)00025-4; pmid: 10967353
54. L. Yan *et al.*, Exploring spatiotemporal organization of SCN circuits. *Cold Spring Harb. Symp. Quant. Biol.* **72**, 527–541 (2007). doi: 10.1101/sqb.2007.72.037; pmid: 18419312
55. J. A. Evans, T. L. Leise, O. Castanon-Cervantes, A. J. Davidson, Intrinsic regulation of spatiotemporal organization within the suprachiasmatic nucleus. *PLOS ONE* **6**, e15869 (2011). doi: 10.1371/journal.pone.0015869; pmid: 21249213
56. R. Enoki *et al.*, Topological specificity and hierarchical network of the circadian calcium rhythm in the suprachiasmatic nucleus. *Proc. Natl. Acad. Sci. U.S.A.* **109**, 21498–21503 (2012). doi: 10.1073/pnas.1214415110; pmid: 23213253
57. M. Brancaccio, E. S. Maywood, J. E. Chesham, A. S. I. Loudon, M. H. Hastings, A Gq-Ca2+ axis controls circuit-level encoding of circadian time in the suprachiasmatic nucleus. *Neuron* **78**, 714–728 (2013). doi: 10.1016/j.neuron.2013.03.011; pmid: 23623697
58. B. E. Jones, Arousal and sleep circuits. *Neuropsychopharmacology* **45**, 6–20 (2020). doi: 10.1038/s41386-019-0444-2; pmid: 31216564
59. P. Franken, D.-J. Dijk, Sleep and circadian rhythmicity as entangled processes serving homeostasis. *Nat. Rev. Neurosci.* **25**, 43–59 (2024). doi: 10.1038/s41583-023-00764-z; pmid: 38040815
60. E. M. Ko, I. V. Estabrooke, M. McCarthy, T. E. Scammell, Wake-related activity of tuberomammillary neurons in rats. *Brain Res.* **992**, 220–226 (2003). doi: 10.1016/j.brainres.2003.08.044; pmid: 14625060
61. T. Kato *et al.*, Oscillatory population-level activity of dorsal raphe serotonergic neurons is inscribed in sleep structure. *J. Neurosci.* **42**, 7244–7255 (2022). doi: 10.1523/JNEUROSCI.2288-21.2022; pmid: 35970565
62. I. V. Estabrooke *et al.*, Fos expression in orexin neurons varies with behavioral state. *J. Neurosci.* **21**, 1656–1662 (2001). doi: 10.1523/JNEUROSCI.21-05-01656.2001; pmid: 11222656
63. M. Xu *et al.*, Basal forebrain circuit for sleep-wake control. *Nat. Neurosci.* **18**, 1641–1647 (2015). doi: 10.1038/nn.4143; pmid: 26457552
64. C. Cajochen, J. K. Wyatt, C. A. Czeisler, D. J. Dijk, Separation of circadian and wake duration-dependent modulation of EEG activation during wakefulness. *Neuroscience* **114**, 1047–1060 (2002). doi: 10.1016/S0306-4522(02)00209-9; pmid: 12379258
65. D. Ono *et al.*, The mammalian circadian pacemaker regulates wakefulness via CRF neurons in the paraventricular nucleus of the hypothalamus. *Sci. Adv.* **6**, eabd0384 (2020). doi: 10.1126/sciadv.abd0384; pmid: 33158870
66. M. H. Qiu, M. C. Chen, P. M. Fuller, J. Lu, Stimulation of the pontine parabrachial nucleus promotes wakefulness via extra-thalamic forebrain circuit nodes. *Curr. Biol.* **26**, 2301–2312 (2016). doi: 10.1016/j.cub.2016.07.054; pmid: 27546576
67. J. K. Leutgeb, S. Leutgeb, M.-B. Moser, E. I. Moser, Pattern separation in the dentate gyrus and CA3 of the hippocampus. *Science* **315**, 961–966 (2007). doi: 10.1126/science.1135801; pmid: 17303747
68. D. Chaudhury, L. M. Wang, C. S. Colwell, Circadian regulation of hippocampal long-term potentiation. *J. Biol. Rhythms* **20**, 225–236 (2005). doi: 10.1177/0748730405276352; pmid: 15851529
69. S. M. Montgomery, A. Sirota, G. Buzsáki, Theta and gamma coordination of hippocampal networks during waking and rapid eye movement sleep. *J. Neurosci.* **28**, 6731–6741 (2008). doi: 10.1523/JNEUROSCI.1227-08.2008; pmid: 18579747
70. J. S. Farrell, E. Hwaun, B. Dudok, I. Soltesz, Neural and behavioural state switching during hippocampal dentate spikes. *Nature* **628**, 590–595 (2024). doi: 10.1038/s41586-024-07192-8; pmid: 38480889
71. Y. Senzai, G. Buzsáki, Physiological properties and behavioral correlates of hippocampal granule cells and mossy cells. *Neuron* **93**, 691–704.e5 (2017). doi: 10.1016/j.neuron.2016.12.011; pmid: 28132824
72. C. A. Barnes, B. L. McNaughton, G. V. Goddard, R. M. Douglas, R. Adamec, Circadian rhythm of synaptic excitability in rat and monkey central nervous system. *Science* **197**, 91–92 (1977). doi: 10.1126/science.194313; pmid: 194313
73. Z. Yao *et al.*, A taxonomy of transcriptomic cell types across the isocortex and hippocampal formation. *Cell* **184**, 3222–3241.e26 (2021). doi: 10.1016/j.cell.2021.04.021; pmid: 34004146
74. M. S. Cembrowski *et al.*, Spatial gene-expression gradients underlie prominent heterogeneity of CA1 pyramidal neurons. *Neuron* **89**, 351–368 (2016). doi: 10.1016/j.neuron.2015.12.013; pmid: 26777276
75. L. K. Goode *et al.*, Examination of diurnal variation and sex differences in hippocampal neurophysiology and spatial memory. *eNeuro* **9**, ENEURO.0124-22.2022 (2022). doi: 10.1523/ENEURO.0124-22.2022; pmid: 36265903
76. E. L. Hargreaves, G. Rao, I. Lee, J. J. Knierim, Major dissociation between medial and lateral entorhinal input to dorsal hippocampus. *Science* **308**, 1792–1794 (2005). doi: 10.1126/science.1110449; pmid: 15961670
77. A. Tsao *et al.*, Integrating time from experience in the lateral entorhinal cortex. *Nature* **561**, 57–62 (2018). doi: 10.1038/s41586-018-0459-6; pmid: 30158699
78. K. Roybal *et al.*, Mania-like behavior induced by disruption of CLOCK. *Proc. Natl. Acad. Sci. U.S.A.* **104**, 6406–6411 (2007). doi: 10.1073/pnas.0609625104; pmid: 17379666
79. C. B. Canto, Y. Onuki, B. Bruinsma, Y. D. van der Werf, C. I. De Zeeuw, The sleeping cerebellum. *Trends Neurosci.* **40**, 309–323 (2017). doi: 10.1016/j.tins.2017.03.001; pmid: 28431742
80. W. M. Usrey, S. M. Sherman, Corticofugal circuits: Communication lines from the cortex to the rest of the brain. *J. Comp. Neurol.* **527**, 640–650 (2019). doi: 10.1002/cne.24423; pmid: 29524229
81. E. Trudel, C. W. Bourque, Circadian modulation of osmoregulated firing in rat supraoptic nucleus neurones. *J. Neuroendocrinol.* **24**, 577–586 (2012). doi: 10.1111/j.1365-2826.2012.02298.x; pmid: 22330181
82. L. Talamanca, C. Gobet, F. Naef, Sex-dimorphic and age-dependent organization of 24-hour gene expression rhythms in humans. *Science* **379**, 478–483 (2023). doi: 10.1126/science.add0846; pmid: 36730411
83. S. W. Oh *et al.*, A mesoscale connectome of the mouse brain. *Nature* **508**, 207–214 (2014). doi: 10.1038/nature13186; pmid: 24695228
84. H. Shi *et al.*, Spatial atlas of the mouse central nervous system at molecular resolution. *Nature* **622**, 552–561 (2023). doi: 10.1038/s41586-023-06569-5; pmid: 37758947
85. C. Wang *et al.*, Circadian tumor infiltration and function of CD8^{+} T cells dictate immunotherapy efficacy. *Cell* **187**, 2690–2702.e17 (2024). doi: 10.1016/j.cell.2024.04.015; pmid: 38723627
86. A. Karaboué *et al.*, Why does circadian timing of administration matter for immune checkpoint inhibitors' efficacy? *Br. J. Cancer* **131**, 783–796 (2024). doi: 10.1038/s41416-024-02704-9; pmid: 38834742
87. S. Silva, J. Bicker, A. Falcão, A. Fortuna, Antidepressants and circadian rhythm: Exploring their bidirectional interaction for the treatment of depression. *Pharmaceutics* **13**, 1975 (2021). doi: 10.3390/pharmaceutics13111975; pmid: 34834391
88. A.-S. Perrin-Terrin *et al.*, The c-FOS protein immunohistological detection: A useful tool as a marker of central pathways involved in specific physiological responses in vivo and ex vivo. *J. Vis. Exp.* (110): 53613 (2016). doi: 10.3791/53613; pmid: 27167092

89. S. Y. Lara Aparicio *et al.*, Current opinion on the use of c-Fos in neuroscience. *NeuroSci* **3**, 687–702 (2022). doi: 10.3390/neurosci3040050; pmid: 39483772
90. C. Cirelli, G. Tononi, On the functional significance of c-fos induction during the sleep-waking cycle. *Sleep* **23**, 453–469 (2000). doi: 10.1093/sleep/23.4.9; pmid: 10875553
91. G. A. Sunagawa *et al.*, Mammalian reverse genetics without crossing reveals Nr3a as a short-sleeper gene. *Cell Rep.* **14**, 662–677 (2016). doi: 10.1016/j.celrep.2015.12.052; pmid: 26774482
92. F. Akiyama *et al.*, A multiwell plate approach to increase the sample throughput during tissue clearing. *Nat. Protoc.* **20**, 967–988 (2025). doi: 10.1038/s41596-024-01080-1; pmid: 39627541
93. L. B. Lucy, An iterative technique for the rectification of observed distributions. *Astron. J.* **79**, 745 (1974). doi: 10.1086/111605
94. J. K. Chung, P. L. Kannappan, C. T. Ng, P. K. Sahoo, Measures of distance between probability distributions. *J. Math. Anal. Appl.* **138**, 280–292 (1989). doi: 10.1016/0022-247X(89)90335-1
95. S. Nowozin, B. Cseke, R. Tomioka, f-GAN: Training generative neural samplers using variational divergence minimization. arXiv:1606.00709 [stat.ML] (2016).
96. B. B. Avants *et al.*, A reproducible evaluation of ANTs similarity metric performance in brain image registration. *Neuroimage* **54**, 2033–2044 (2011). doi: 10.1016/j.neuroimage.2010.09.025; pmid: 20851191
97. K. Matsumoto *et al.*, Advanced CUBIC tissue clearing for whole-organ cell profiling. *Nat. Protoc.* **14**, 3506–3537 (2019). doi: 10.1038/s41596-019-0240-9; pmid: 31748753
98. R. A. Fisher, Tests of significance in harmonic analysis. *Proc. R. Soc. Lond., A Contain. Pap. Math. Phys. Character* **125**, 54–59 (1929). doi: 10.1098/rspa.1929.0151
99. R. G. Yamada, “analytic_cosinor (v1.0.2),” Zenodo (2025); https://doi.org/10.5281/zenodo.17418382.
100. F. L. Kinoshita, K. Yamashita, “cfos_circadian (v1.0.2),” Zenodo (2025); https://doi.org/10.5281/zenodo.17421202.

ACKNOWLEDGMENTS

We thank staff at RIKEN, the University of Tokyo, and Kurume University, particularly M. Neus Ballester Roig, for a critical review of the manuscript and figures, as well as K. L. Ode for assistance with constructing the open-access database. We are also grateful to E. A. Susaki (Juntendo University) for advice on the CUBIC protocols and to D. Perrin (Queensland University of Technology) and H. Yukinaga (University of Hyogo) for assistance with early sampling experiments; R. Narumi, K. Tominaga, and T. Nakano (all University of Osaka), V. Mongrain (Université de Montréal), D.-J. Dijk (University of Surrey), A. Jagannath and R. Foster (both University of Oxford), and D. Ray and R. Lukas (both University of Manchester) for discussions on the interpretation of the results. **Funding:** This work was supported by JST ERATO grant JPMJER2001 (H.R.U.); Science and Technology Platform Program for Advanced Biological Medicine (AMED) JP20am0401011 (H.R.U.); JSPS KAKENHI Grant-in-Aid for Scientific Research (C) (JP20K06885 to K.M.); JST Moonshot R&D Program JPMJMS2023 (K.M., R.G.Y.); MEXT Quantum Leap Flagship Program (MEXT QLEAP) (JPMXS0120330644 to H.R.U.); Grants-in-Aid from the Human Frontier Science Program RGP0019/2018 (H.R.U.); JSPS KAKENHI Grant-in-Aid for Scientific Research (S) JP18H05270 (H.R.U.); Intramural Grant-in-Aid from the RIKEN Center for Biosystems Dynamics Research (H.R.U.); JST BOOST JPMJBS2402 (K.Y.); JST SPRING JPMJSP2138 (F.L.K.); the RIKEN Junior Research Associate Program (F.L.K.); JSPS KAKENHI Grant-in-Aid for Early-Career Scientists JP20K16626 (S.Y.Y.); JSPS KAKENHI Grant-in-Aid for Early-Career Scientists JP20K16498 (T.T.M.); JSPS KAKENHI Grant-in-Aid for Scientific Research (C) JP25K10180 (T.T.M.); JST ACT-X JPMJAX242I (T.T.M.); Grant-in-Aid for International Academic Exchange Program from the Osaka University Medical School Alumni (T.T.M.); Takeda Science Foundation (T.T.M.). **Author contributions:** Conceptualization: K.Y., S.Y.Y., K.M., E.M., S.O., H.R.U.; Formal analysis: K.Y., F.L.K., R.G.Y.; Investigation: K.Y., S.Y.Y.; Methodology: K.Y., S.Y.Y., K.M., H.F., Y.M., R.G.Y.; Project administration: H.R.U.; Software: K.M., T.T.M., R.G.Y.; Supervision: H.R.U.; Visualization: K.Y., F.L.K., R.G.Y.; Writing – original draft: K.Y., F.L.K., R.G.Y.; Writing – review & editing: K.Y., R.G.Y., H.R.U. **Competing interests:** H.R.U. has filed a patent application (PCT/JP2014/070618, 2013-168705) related to the CUBIC reagents. H.R.U. is the founder and an equity holder of CUBICStars Inc. and K.M. is also an equity holder. S.Y.Y. is a part-time employee of CUBICStars Inc. The remaining authors declare no competing interests. **Data, code, and materials availability:** An online database for whole-brain circadian neural activity is available at https://circadian.cfosdb.systems-based-medicine.org/database. The code used for data analysis is archived at Zenodo (*100*). Details of the analytic cosinor test are archived at Zenodo (*99*). All other data supporting the findings of this study are available in the main text or the supplementary materials. **License information:**

SUPPLEMENTARY MATERIALS

science.org/doi/10.1126/science.aea3381
Figs. S1 to S29; Tables S1 to S8; Movies S1 and S2; MDAR Reproducibility Checklist

Submitted 7 July 2025; accepted 28 October 2025; published online 13 November 2025

10.1126/science.aea3381

A whole-brain single-cell atlas of circadian neural activity in mice

Katsunari Yamashita, Fukuaki L. Kinoshita, Shota Y. Yoshida, Katsuhiko Matsumoto, Tomoki T. Mitani, Hiroshi Fujishima, Yoichi Minami, Eiichi Morii, Rikuhiro G. Yamada, Seiji Okada, and Hiroki R. Ueda

Science **391** (6787), eaea3381. DOI: 10.1126/science.aea3381

Editor's summary

Although circadian rhythms have been well studied in a few specific regions, their brainwide organization remains poorly understood. To quantify spontaneous circadian neural activity at single-cell resolution, Yamashita *et al*. used tissue clearing and whole-brain immunostaining on a large number of mouse brains over two full circadian cycles. Circadian rhythmicity was present in many brain regions. The activity of most regions peaked during the animals' active phase. However, sleep centers, visual areas, the dentate gyrus, and the cerebellum all peaked during the inactive phase. A closer look revealed distinct circadian phases even within individual regions, highlighting temporal heterogeneity. These findings will be useful for relating physiological and behavioral experimental data to the time-of-day–driven internal regulatory forces. —Peter Stern

Science (ISSN 1095-9203) is published by the American Association for the Advancement of Science. 1200 New York Avenue NW, Washington, DC 20005. The title *Science* is a registered trademark of AAAS.